

Probabilistic Seismic Source Inversion of the 1886 Charleston, South Carolina, Earthquake from Macroseismic Evidence: A Major Updating

Rasanen, R.A.^a and Maurer, B.W.^{a,*}

ABSTRACT

The source of the 1886 Charleston, South Carolina earthquake influences the computed seismic hazard of the Southeastern U.S. and thus impacts public policy and engineering practice. However, because the 1886 rupture predated seismic instruments, its source is highly uncertain. This study presents probabilistic seismic-source inversions of the Charleston earthquake from liquefaction evidence and historical intensity reports. Using the latest predictive models and a novel inversion approach, we seek to constrain the magnitude, location, and orientation of the 1886 rupture. Probability distributions of rupture magnitude are conditioned on both the “Woodstock Fault” – a commonly inferred source of the 1886 event – and on an unknown source, wherein the uncertainties of fault location and orientation are considered. These distributions are compared to the $M_w 6.7$ - $M_w 7.5$ distribution adopted by the U.S. National Seismic Hazard Model Project (NSHMP). Collectively, the results do not provide strong support for the hypothesized Woodstock Fault. This is not to say the Woodstock Fault does not exist, but rather, that the position of the 1886 source model cannot be constrained by the data and models studied herein, given the large uncertainties inherent to each. While this is at odds with the underlying assumption of many prior studies, the results nonetheless generally uphold the magnitude distribution assumed by the NSHMP. The largest uncertainties inherent to this distribution are identified and could be diminished in the future. Finally, we note that the inversion methodology used here is not specific to any region, or to certain types of evidence, but can be applied to any seismic zone and to any co-seismic response. This methodology allows for uncertainty to be accounted for in a more complete and transparent manner when inverting seismic source parameters from macroseismic data. Of course, any limitations, biases, or unmodeled uncertainties inherent to these data must be understood, and their implications acknowledged, as further discussed herein.

Keywords: seismic hazard, macroseismic intensity, soil liquefaction, inverse analysis

1. Introduction

Computed seismic hazards are especially uncertain in regions of infrequent seismicity, where the return periods of moderate-to-large earthquakes may exceed the historic observational period. To reduce this uncertainty, engineering geologists routinely perform forensic analyses of the macroseismic evidence (e.g., liquefaction, landslides, intensity reports) produced by prehistoric and pre-instrumental earthquakes (e.g.,

^a Department of Civil and Environmental Engineering, University of Washington, Seattle, Washington 98195

*Corresponding author: bwmaurer@uw.edu

among many, Obermeier et al., 1998; Schneider et al., 2001; Green et al., 2005; Kuhn, 2005; Obermeier et al., 2005; Olson et al., 2005; Rodriguez-Marek and Ciani, 2008; Maurer et al., 2015a; Gheibi and Gassman, 2016; Yousuf et al., 2021; Chung et al., 2021; Rasanen et al., 2021; Bwambale et al., 2022). The goal of these analyses, in effect, is to constrain the seismic-source parameters of paleoearthquakes, such that these parameters may be input to probabilistic seismic hazard analyses. It follows that computed seismic hazards are, in some regions, heavily influenced by analyses of macroseismic evidence. The South Carolina Coastal Plain is one such region and is strongly influenced by interpretations of the 1886 Charleston earthquake.

The 1886 event induced widespread soil liquefaction across the Coastal Plain (Amick et al., 1990), damaged structures in multiple U.S. states, including most structures in Charleston (Dutton, 1889; Wong et al., 2005), produced perceptible shaking over 1500 km away in Canada (Bakun et al., 2002), and was larger in magnitude than any earthquake to since occur in the Southeastern U.S. The source of the Charleston event is thus a major seismic hazard for the region. A 2005 study, for example, predicted that a repeat of the 1886 event would cause 900 deaths, 44,000 injuries, and economic losses of \$20 billion in South Carolina alone (Wong et al., 2005). In turn, the Charleston source controls the computed seismic hazard for much of the Southeastern U.S., particularly for long-period structures (Petersen et al., 2020), and thus impacts building codes, governing policies, and engineering practice. However, because the 1886 rupture predated seismic instruments and did not manifest at the surface, its exact location and magnitude remain uncertain, as do the regional amplitudes of resultant ground motions. To constrain these unknowns, and thus prepare for a similar event, numerous researchers have studied macroseismic evidence, as summarized in Table 1. Published confidence intervals (CIs) of the 1886 magnitude range from $M_w6.4$ to $M_w7.8$, as interpreted from intensity reports (e.g., Bakun and Hopper, 2004; Cramer and Boyd, 2014) and liquefaction evidence (e.g., Martin and Clough, 1994; Hayati and Andrus, 2008). Liquefaction features also suggest a history of recurrent earthquakes in the region extending back 6,000 years (Talwani and Schaeffer, 2001) with wide-ranging magnitude estimates of $M_w5.1$ to $M_w7.8$ (e.g., Hu et al., 2002; Gheibi et al., 2020). Considering the existing literature, Petersen et al. (2014, 2020) assigned to the Charleston seismic zone a magnitude probability distribution that ranged from $M_w6.7$ to $M_w7.5$ in the most recent U.S. National Seismic Hazard Model Project (NSHMP) maps.

While much has been learned about the 1886 Charleston earthquake, prior analyses of the macroseismic data (i.e., intensity reports, soil liquefaction) have several limitations. First, the analysis of this data has multiple uncertainties, yet existing studies tend either to be deterministic or to account for uncertainties informally. That is, they generally provide either a median estimate of the rupture magnitude or uncertainty bounds that are nominal in nature. It is often unclear what the bounds are, exactly, and which uncertainties are, and are not, accounted for. Second, most analyses assume that the 1886 event was caused by a particular fault (i.e., the “Woodstock Fault”) with known characteristics, even though the fault(s) responsible for the

event are debated and the characteristics of the Woodstock Fault are uncertain. The feasibility of the data to constrain the source model has arguably not been fully explored, given that nearly all studies provide a magnitude estimate conditioned on a single fault and do not investigate the uncertainty of this assumption. Third, the inverse analysis of intensity and liquefaction data requires a series of models for predicting these phenomena. Regionally distributed ground motions must be predicted, conditioned on a hypothetical source, to include site-response effects at the locations of study. The probability of field observations (i.e., the observed intensity or liquefaction response) must then be computed, conditioned on the expected ground motions. In this regard, major modeling advances have recently been made. The NGA-East project (Goulet et al., 2018) resulted in the most advanced understanding of Eastern North America (ENA) ground motions and site response (Harmon et al., 2019) to date. Models for correlating ground motions to macroseismic intensities, including ENA-specific relationships, have been updated (e.g., Cramer, 2020). And models for predicting the probability of liquefaction surface expression have been trained using all liquefaction case histories globally compiled to date (Geyin and Maurer, 2020).

Table 1. Prior estimates of the 1886 Charleston earthquake magnitude; estimates are in moment magnitude (M_w) and ranges are at the 95% confidence level, unless noted otherwise (m_b = body wave magnitude; M_s = surface wave magnitude).

Study	Study Type	Magnitude
Bollinger (1977)	MMI	6.8-7.1 (m_b)*
Nuttli et al. (1986)	MMI	6.7 (m_b), 7.7 (M_s)†
Martin and Clough (1994)	Liquefaction	7.0-7.5†
Johnston (1996)	MMI	6.8-7.8
Bakun and Hopper (2004)	MMI	6.4-7.2
Heidari and Andrus (2010)	Liquefaction	6.8-7.0†
Cramer and Boyd (2014)	MMI	6.7-7.3

* Upper bound magnitude estimate (range is not at the 95% confidence level)

† Magnitude range is either not given or is not at the 95% confidence level

Accordingly, this study presents probabilistic seismic-source inversions of the 1886 Charleston earthquake from historical intensity reports and liquefaction evidence. Each is studied using a novel approach wherein the above shortcomings are addressed directly. With this approach, the likelihood of a rupture with some location, geometry, and magnitude to produce a set of field observations (observed intensities or liquefaction responses) is computed. Repeating for enumerable hypothetical faults results in a regional scale understanding of the likely source parameters, to the degree the observational data permits. Probability distributions of earthquake magnitude, conditioned on both an unknown source and on the Woodstock Fault, are computed and compared to that used to develop the NSHMP maps (Petersen et al., 2014, 2020). In the following, prior studies of the 1886 macroseismic data are summarized. An overview

of the analysis methodology is then presented, followed by implementation details. Lastly, the macroseismic data are analyzed and a variety of results are presented and discussed.

2. Prior analyses of 1886 macroseismic evidence

2.1 Analyses of MMI data

Following the 1886 earthquake, Dutton (1889) compiled intensity reports throughout ENA and developed isoseismal maps based on the Rossi-Forel intensity scale. Researchers have since reinterpreted these reports to the Modified Mercalli Intensity (MMI) scale and analyzed them to infer seismic parameters. Bakun et al. (2002), for example, compiled 1,034 MMI observations from these and other original reports. Prior analyses of the 1886 MMI data have typically used intensity-prediction equations (IPEs), which predict intensity as a function of rupture magnitude and site-to-source distance. Assuming some source location and adopting an IPE, researchers have constrained the causative M_w which best fits the MMI data (e.g., Bollinger, 1977; Nuttli et al., 1986; Johnston, 1996; Bakun and Hopper, 2004) as summarized in Table 1. Bakun and Hopper (2004), for example, developed an ENA-specific IPE, applied it to the Bakun et al. (2002) MMI data, and reported a magnitude of $M_w 6.9$ ($M_w 6.4-7.2$ at the 95% confidence level). Using different methods than prior researchers, Cramer and Boyd (2014) compared the mean MMI of the Bakun et al. (2002) dataset against those from two reference events in similar tectonic settings ($M_w 7.2$ 1929 Grand Banks, Canada and $M_w 7.6$ 2001 Bhuj, India) over a site-to-source distance of 600-1200 km. With this approach, Cramer and Boyd (2014) estimated a median magnitude of $M_w 7.0$ with uncertainty of $\pm 0.3 M_w$. Collectively, existing studies of the MMI data have reported estimates of $M_w 6.4$ to $M_w 7.8$. In producing such estimates, these studies have generally assumed that the source was epicentrally located in the vicinity of what is typically called the Woodstock Fault, an inferred N striking, W dipping fault ~25 km NW of Charleston (e.g., Durá-Gómez and Talwani, 2009a,b; Chapman et al., 2016). The fault's surface projection, as hypothesized by Durá-Gómez and Talwani (2009a,b), is mapped in Figure 1. While most studies based on geophysical investigations or modern seismological data have supported this proposed alignment – at least in a general sense (e.g., Pratt et al., 2022) – dramatically different hypotheses for the 1886 earthquake have also been proposed. Marple and Hurd (2020), for example, recently suggested that the 40-km long “Deer Park lineament,” which is oriented roughly E-W, may have been responsible.

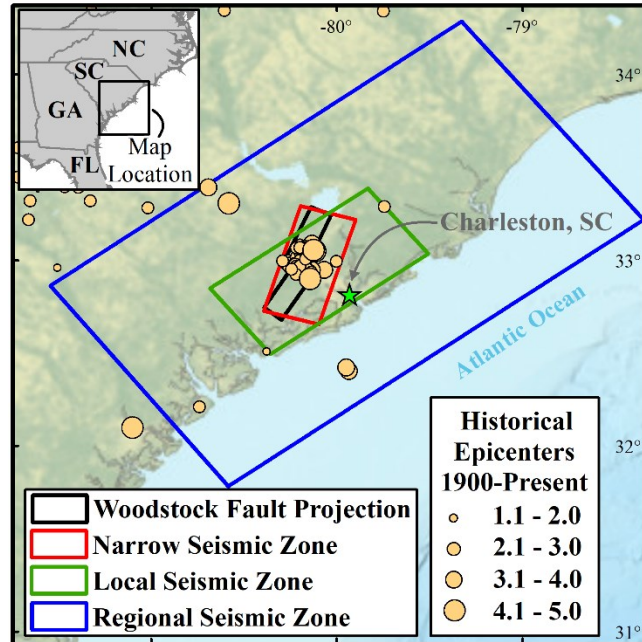


Figure 1. Woodstock Fault projection (Durá-Gómez and Talwani, 2009a,b) and the zonal weighting scheme assigned to the Charleston Seismic Zone in the most recent U.S. National Seismic Hazard Model Project (NSHMP) maps (Petersen et al., 2014, 2020).

Also shown in Figure 1 is the zonal weighting scheme assigned to the Charleston Seismic Zone by the NSHMP (Petersen et al., 2014, 2020). In this scheme, a “Narrow” zone with weight of 0.3 delineates the hypothesized Woodstock Fault while accounting for uncertainties in its position and branching structure. The “Local” and “Regional” zones, with respective weights of 0.5 and 0.2, collectively extend offshore and across the extents of the South Carolina Coastal Plain, thereby encompassing more distal faults and liquefaction features that have not been tied to the 1886 event. Each zone is assigned the same M_w 6.7 to M_w 7.5 probability distribution by Petersen et al. (2014, 2020). This weighting scheme was adopted from the Central and Eastern United States Seismic Source Characterization for Nuclear Facilities Project (Coppersmith et al., 2012), who concluded: “Neither the 1886 nor the prehistoric (i.e., pre-1886) earthquakes in the Charleston area can be definitively attributed to any specific fault or fault zone at the present time.” In arriving at this conclusion, Coppersmith et al. (2012) noted: “the Charleston region is associated with a pattern of observed seismicity that is not particularly remarkable for drawing attention to the location of the 1886 earthquake.” While it should be emphasized that the NSHMP weighting scheme does not describe the uncertainty of the 1886 earthquake specifically, it does reflect the overall uncertainty of moderate-to-large “1886-like” earthquakes in the region. Thus, while prior studies have generally assumed that the 1886 source was in the “Narrow” zone, a scientific consensus has not been reached.

As a precursor to other analyses presented herein, the Bakun and Hopper (2004) IPE was first reimplemented on the Bakun et al. (2002) dataset and the same $M_w 6.9$ estimate as Bakun and Hopper (2004) was obtained, indicating that the approach and dataset were correctly reproduced. Next, this approach was updated using the newest ENA IPE (Atkinson et al., 2014). Assuming the same source location and studying MMI data within 1000 km (the applicable distance of the Atkinson et al. (2014) IPE) and within all distances (to mirror Bakun and Hopper, 2004), median estimates of $M_w 8.0$ and $M_w 8.2$ were respectively obtained. The cause of the discrepant results obtained using Bakun and Hopper (2004) vs. Atkinson et al. (2014) can be seen in Figure 2, where both IPEs are plotted for three values of M_w . For a given M_w and epicentral distance, the Atkinson et al. (2014) model tends to predict a lesser MMI, indicating that a larger earthquake magnitude (i.e., $M_w 8.0 - M_w 8.2$) is needed to produce the same set of MMI observations.

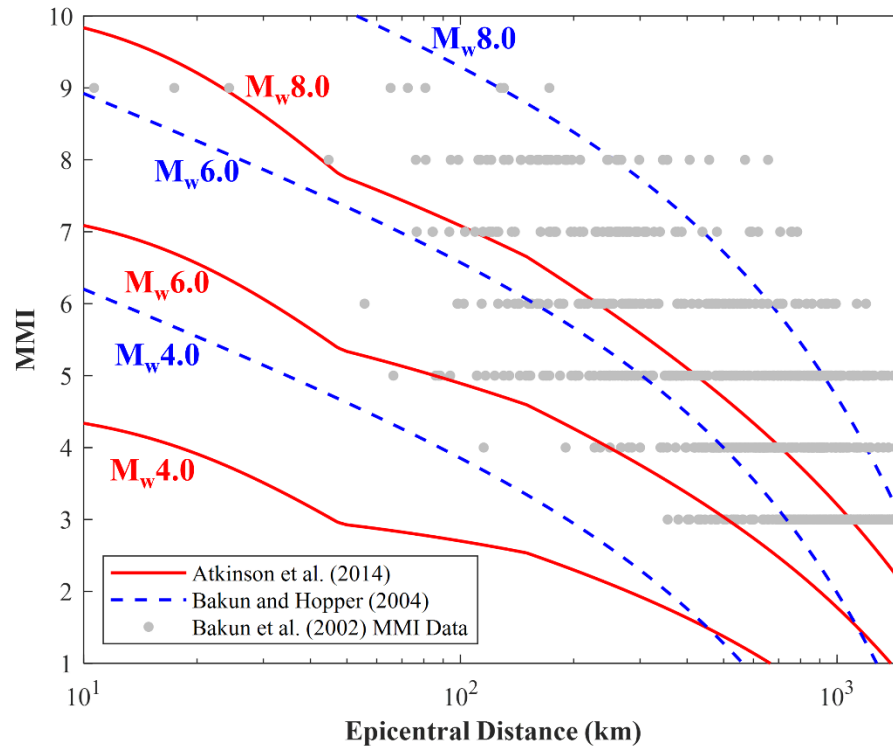


Figure 2. ENA-specific intensity prediction equations (IPEs) proposed by Bakun and Hopper (2004) and Atkinson et al. (2014) considering three values of M_w .

While it may appear, per the latest ENA IPE, that the 1886 rupture was much larger than previously thought, there are limitations that give rise to the work that follows. Most notably, perhaps, is that existing ENA IPEs do not allow for consideration of site effects when predicting MMI. The Atkinson et al. (2014) IPE, for example, is intended for site class C conditions (i.e., stiff soils). Accordingly, if some of the 1886 MMI observations were on softer sites (e.g., in river valleys or along waterways, which seems likely), then the estimate of $M_w 8.0 - M_w 8.2$ obtained via the Atkinson et al. (2014) IPE could require significant reduction.

Moreover, the MMI studies in Table 1: (i) predate the latest knowledge of ENA ground motions and site response (Goulet et al., 2018; Harmon et al., 2019); and (ii) do not rigorously account for uncertainty. In this study, probabilistic site-adjusted ground motion intensity measures (IMs) will be explicitly predicted using 17 ENA ground-motion models (GMMs) (whereas ground motions were only implicitly predicted in prior studies). In turn, MMI values will be probabilistically predicted at study sites using the latest IM-MMI models (e.g., Cramer, 2020). These predictions will be repeated for a multitude of fault locations, orientations, and magnitudes to compute the likelihood that each source would produce the 1886 MMI observations of Bakun et al. (2002). This approach, which will be subsequently presented in detail, incorporates ground-motion IM uncertainty, IM-MMI uncertainty, and source location uncertainty to produce a probability distribution of rupture magnitude. It must be noted that MMI data is also subject to measurement uncertainty and reporting bias (e.g., Hough et al., 2000; Cramer and Boyd, 2014). While site-specific measurement uncertainties, correction factors, or weighting schemes could be accommodated, a thorough reinterpretation of the more than 1000 original intensity reports would be required, to include possible reassignment of MMI values in the Bakun et al. (2002) dataset and development of observation-specific uncertainties. In the current effort, however, we study the existing data directly, treat measurement uncertainty in a simple manner, and assign all observations equal weight. It should be noted that all prior studies of the 1886 intensities have also used these data. Thus, while our methodology has important advantages over prior efforts (e.g., the capacity to probabilistically constrain the rupture location), a future study might further benefit from rigorous reinterpretation of the original intensity reports.

2.2 Analyses using liquefaction

Paleoliquefaction evidence suggests that at least seven moderate-to-large earthquakes have impacted the South Carolina Coastal Plain in the last 6,000 years (e.g., Gohn et al., 1984; Obermeier et al., 1985; Obermeier et al., 1987; Talwani and Schaeffer, 2001). Three of these events are interpreted to have a source in the vicinity of Charleston and a recurrence rate of ~500 years (Talwani and Schaeffer, 2001). The 1886 event was the most recent of these to generate liquefaction and the only instance in which liquefaction was well documented as it occurred. Surface manifestations (e.g., ejecta, ground cracks) were mapped by Earle Sloan, among others, and compiled by Dutton (1889). Additional liquefaction evidence was subsequently discovered during trenching investigations (e.g., Obermeier et al., 1985; Talwani and Cox, 1985). Collectively, this evidence has been analyzed to determine the magnitude of the earthquake that caused it. Liquefaction models (e.g., Green et al., 2019; Maurer et al., 2015b) conventionally predict the future triggering and surface manifestation of liquefaction, given in-situ geotechnical test data and some seismic loading. In an inverse analysis, these models are used in reverse to constrain the seismic loading that would, and would not, produce the observed response. By comparing this loading to that forward predicted by a

GMM for an assumed source, the magnitude of that source may be constrained. Studying primarily standard penetration test (SPT) data from sites of interest, Martin and Clough (1994) carried out such an analysis with the Seed et al. (1984) SPT-based liquefaction triggering model and the Ishihara (1985) liquefaction manifestation model. Assuming a seismic source at the centroid of reported intensity (roughly consistent with the hypothesized Woodstock Fault), adopting GMMs then available (e.g., Chapman et al., 1989), and employing considerable judgement, Martin and Clough (1994) estimated that an $M_w7.0$ - $M_w7.5$ event could produce liquefaction consistent with that observed.

Studying cone penetration test (CPT) data, Hayati and Andrus (2008) used the Robertson and Wride (1998) CPT-based triggering model and the Iwasaki et al. (1978) manifestation model to estimate a magnitude of $M_w6.8$ - $M_w7.3$. Because triggering models are trained almost exclusively with case-history data from Holocene deposits, “aging correction” factors (or “deposit resistance” corrections) have been proposed when applying triggering models in older soils. Specifically, it has been argued that aging effects, or increases in the cyclic strength of soils over time, may be resolved into gains measurable by large strain penetration tests and gains influenced by soil fabric phenomena undetectable at larger strain (e.g., Maurer et al., 2014). Thus, penetration resistance may correlate to liquefaction resistance differently in Pleistocene soils than in Holocene soils. Accordingly, Hayati and Andrus (2008) employed aging correction factors in select geologic units. In producing their estimate of $M_w6.8$ - $M_w7.3$, Hayati and Andrus (2008) assumed that the Woodstock fault was the source and that a peak ground acceleration (*PGA*) of 0.3 g occurred throughout Charleston, citing previous ground-motion predictions (e.g., Silva et al., 2003). Using this methodology, they constrained the magnitude range for which predictions from liquefaction models matched observations of response. Heidari and Andrus (2010) used a similar methodology as Hayati and Andrus (2008) but applied the updated aging correction factors of Hayati and Andrus (2009) to obtain an estimate of $M_w6.8$ - $M_w7.0$. In addition to these studies, researchers have studied paleoliquefaction interpreted to be from older, possibly similar events. Gheibi et al. (2020), for example, studied evidence induced by a “Charleston Source” approximately ~550 and ~5,000 YBP. Assuming the source to be the Woodstock fault, they computed respective minimum magnitudes of $M_w6.6$ - $M_w7.2$ and $M_w6.2$ - $M_w6.7$ for these two events, where the uncertainty stems from which GMM is adopted to predict median ground motions.

Like prior studies of the MMI data, those of liquefaction evidence have greatly improved knowledge of the regional seismic hazard, but also have limitations that motivate the present study. In brief, existing studies: (i) predate both the NGA East Project (Goulet et al., 2018; Harmon et al., 2019) and the latest liquefaction models trained on all globally available data (Geyin and Maurer, 2020); and (ii) do not rigorously account for uncertainty. In this regard, prior studies do not account for source-model uncertainty (i.e., they assume a single seismic source), do not account for the uncertainty of ground motions conditioned on that source, and do consider the prediction of liquefaction in any probabilistic sense. In general,

published uncertainties of the 1886 rupture magnitude, whether derived from MMI or liquefaction data, are arguably nominal in nature. In some studies, for example, only a single uncertainty is considered, such as the epistemic uncertainty of which deterministic model is used (say, to compute ground motions). In such cases, published uncertainty bounds (e.g., $M_w 6.8$ - $M_w 7.0$) are ranges of the estimated *median* magnitude considering one source of uncertainty. This may be distinctly different from the total uncertainty of the 1886 magnitude, which could be much greater. Consider, for example, that *instrumental* magnitudes have 95% CIs exceeding some of the ranges in Table 1 (e.g., Werner and Sornette, 2008).

In this study, and analogous to the analysis of MMI data, probabilistic site-adjusted ground motion IMs will be predicted by 17 ENA GMMs. Conditioned on these IMs, the probability of liquefaction manifestation will be computed by the fragility functions of Geyin and Maurer (2020), wherein multiple models for soil aging effects will be ensembled. These predictions will be repeated for a multitude of hypothetical sources to compute the likelihood that each would produce the observed regional liquefaction response. Like the study of MMI data, this will result in a probability distribution of earthquake magnitude and, arguably, a more complete and transparent understanding of the 1886 source model, at least insofar as can be gained from the macroseismic evidence available for analysis.

3. Macrosesimic data

3.1 MMI data

Bakun et al. (2002) compiled 1,034 intensity reports from the 1886 event, including those of Dutton (1889) and Bollinger and Stover (1976), and assigned MMI values per the: (i) MMI definitions of Wood and Neumann (1931); and (ii) USGS National Earthquake Information Center practice for assigning intensity (Stover and Coffman, 1993). In compiling these data, Bakun et al. (2002) either excluded $MMI = 1$ and $MMI = 2$ reports (i.e., documented instances where shaking was not felt) or found no such reports to compile. Like all previous studies of these data, we assume that MMI values were accurately assigned by Bakun et al. (2002), with proper consideration of structural vulnerability to avoid biasing estimates. While matters of MMI uncertainty and bias could be important and will be further discussed, they are largely beyond the scope of the present analysis. It should be emphasized that our analysis is not an endorsement of the Bakun et al. (2002) dataset. Rather, we study this data because it is the most recent compilation of 1886 intensity reports and because many prior publications studied either the Bakun et al. (2002) compilation, or earlier collections of data that Bakun et al. (2002) built upon. As previously stated, a future study could further benefit from a complete reinterpretation of the more than 1000 original intensity reports. While the coordinates of one MMI report from Ottawa, Ontario were judged to be erroneous and corrected by judgement, we otherwise adopt the Bakun et al. (2002) MMI data as presented therein. The locations of these data are shown in Figure 3 and extend ~1500 km from Charleston, SC.

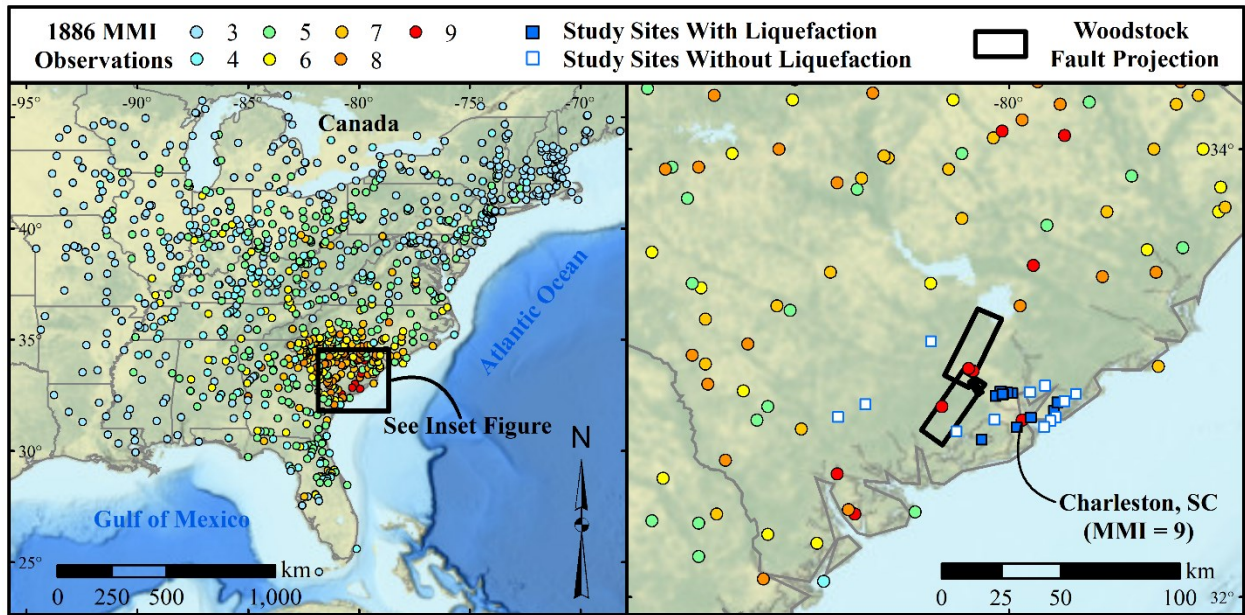


Figure 3. 1886 MMI observations (Bakun et al., 2002) and liquefaction evidence, as introduced subsequently. Also shown is the Woodstock Fault projection (Durá-Gómez and Talwani, 2009a,b).

3.2 Liquefaction data

Twenty-four sites where liquefaction manifestations were or were not observed in 1886, and where CPT testing was subsequently performed, will be studied. Liquefaction manifested (typically in the form of large sand boils) at twelve of these sites, whereas no evidence of liquefaction was observed at the remainder. These sites are summarized in Table 2, where citations are provided for the observed liquefaction response and for the geotechnical tests, which are all available in the public domain. These study sites are also mapped later in the paper.

Table 2. Summary of 1886 liquefaction data analyzed herein.

CPT ID	Longitude	Latitude	Manifestation	Geotechnical Reference	Liquefaction Reference
BKY07	-79.9061	32.9150	No	USGS (2021)	Dutton (1889)
BKY09	-79.8385	32.9443	No	USGS (2021)	Dutton (1889)
BKY23	-79.9855	32.9115	Yes	USGS (2021)	Dutton (1889)
BKY24	-80.0071	32.9118	Yes	USGS (2021)	Dutton (1889)
CHN01	-79.7900	32.8030	No	USGS (2021)	Dutton (1889)
CHN07	-79.8134	32.7874	No	USGS (2021)	Dutton (1889)
CHN12	-79.7989	32.8310	Yes	USGS (2021)	Amick et al. (1990)
CHN15	-79.6998	32.9073	No	USGS (2021)	Dutton (1889)
CHN28	-79.8428	32.7597	No	USGS (2021)	Dutton (1889)
CHN29	-79.7840	32.8682	Yes	USGS (2021)	Amick et al. (1990)
CHN31	-79.7520	32.8741	No	USGS (2021)	Dutton (1889)

CHN32	-80.0267	32.9043	Yes	USGS (2021)	Dutton (1889)
CHN33	-80.0323	32.9166	Yes	USGS (2021)	Dutton (1889)
CHN34	-80.0391	32.9170	Yes	USGS (2021)	Dutton (1889)
CHN50	-80.1235	32.7023	Yes	USGS (2021)	Dutton (1889)
CHN59	-79.9655	32.7575	Yes	USGS (2021)	Dutton (1889)
CHN64	-80.0604	32.8982	Yes	USGS (2021)	Dutton (1889)
CREC1	-80.0655	32.7921	No	Boller (2008)	Martin and Clough (1994); Boller (2008)
FHS3	-80.3507	33.1420	No	Hasek (2016)	Williamson and Gassman (2014); Hasek (2016)
HA74	-80.0300	32.9050	Yes	Heidari & Andrus (2012)	Dutton (1889)
HWD2	-80.2355	32.7394	No	Hasek (2016)	Talwani and Cox (1985); Hasek (2016)
S99634DS1	-79.9015	32.8017	Yes	Heidari & Andrus (2010)	Dutton (1889)
WLC2	-80.6444	32.8607	No	Geiger (2010)	Geiger (2010)
WRAP2	-80.7666	32.8040	No	Geiger (2010)	Geiger (2010)

In compiling these study sites, an interpreted, potential lateral spread at Fort Dorchester, SC (Talwani et al., 2011) was omitted because the liquefaction response was ambiguous and because lateral spreading – a distinct and complex manifestation of liquefaction – is not intended to be predicted by the liquefaction model adopted herein. Whereas the MMI data are spread throughout ENA, the compiled liquefaction data are within 100 km of Charleston. Because liquefaction is mechanistically implausible, irrespective of soil properties, at *PGAs* less than ~ 0.09 g (de Magistris, 2013), the maximum site-to-source distance of liquefaction observations is inherently limited. By corollary, an analysis of sites where liquefaction was not observed, but which are very far from Charleston, would not provide meaningful constraint of the source model, given that the computed probability of such an observation is 100% even for very large earthquakes. In addition, while the MMI data from 1886 are unlikely to grow significantly, additional liquefaction data could be compiled. That is, the liquefaction response was documented in 1886 at more than twenty-four sites, but costly geotechnical testing must also be performed at each site. In this regard, it is known that CPTs have been performed near additional sites of observation, yet these data are privately held and could not be obtained for analysis. Nonetheless, a larger dataset could be studied in the future.

4. Methodology

The methodology that will be used to analyze macroseismic data was first introduced by Rasanen and Maurer (2021, 2022), who collectively demonstrated and validated its use on landslide and liquefaction evidence produced by eleven modern earthquakes with known source models. This is the first application of the method to a prehistoric or pre-instrumental earthquake. The methodology will be covered in two

sections. The first provides a succinct conceptual overview. The second describes in detail the application of the methodology to the 1886 Charleston earthquake.

4.1 Conceptual Overview

Our goal is to probabilistically constrain the 1886 source model. This is accomplished by computing the likelihood that a rupture with some magnitude, location, and geometry, would produce a set of field observations (reported MMI or liquefaction observations), wherein uncertainties inherent to these observed outcomes are considered. In general, the likelihood of a parameter having some value, given a set of observations, is the product of the probabilities of those observations, conditioned on the parameter value. In other words, the likelihood of a rupture having some magnitude (M_w), location (L), and geometry (G), given a set (x) of field observations at N different sites, can be computed as:

$$\text{Likelihood}(L, G, M_w | x) = P(X = x | L, G, M_w) = \prod_{i=1}^N P(X_i = x_i | L, G, M_w) \quad (1)$$

where $P(X_i = x_i | L, G, M_w)$ is the probability of what was observed at site i (i.e., the observed MMI or liquefaction response) given an earthquake with parameters L , G , and M_w . By repeating for enumerable possibilities, the actual rupture parameters may be probabilistically constrained by the likelihood function (product of the probabilities of N observations), such that different source models will be found more and less likely to produce the observed evidence.

If the evidence is MMI data, then the probability of any one field observation (obs) is:

$$P(\text{obs} | \text{EQK}; L, G, M_w) = \int_{IM} \int_{MMI} P(\text{obs} | \text{MMI}) f(\text{MMI} | IM) f(IM | L, G, M_w) \cdot dMMI \cdot dIM \quad (2)$$

where $f(IM | L, G, M_w)$ is the probability of an IM value conditioned on fault parameters L , G and M_w , and site parameter V_{S30} (i.e., the time averaged shear-wave velocity over the upper 30 m), as computed by a GMM that considers site response; $f(\text{MMI} | IM)$ is the probability of an MMI value conditioned on the IM value, and possibly on other parameters, as computed by an IM-MMI model; and $P(\text{obs} | \text{MMI})$ is the binomial probability that the predicted MMI is equal to the observed MMI. In this work, we consider predictions and observations to agree if within ± 0.5 MMI (e.g., predicted MMIs of 5.51 and 6.49 agree with an observed MMI of 6). Thus, we assign an implicit, uniform measurement uncertainty of ± 0.5 MMI, but do not otherwise model the uncertainty of reported MMIs. In this regard, a thorough reinterpretation of the original intensity data, to include assignment of site-specific uncertainty distributions and corrections for bias, would be a valuable endeavor. In the current effort, however, we adopt the Bakun et al. (2002) MMI dataset, which has been studied by other modern investigators of the 1886 earthquake.

If the evidence is observed liquefaction response rather than MMI, then the probability of field observation is computed per Eq (3) if liquefaction manifestation was observed and per Eq (4) otherwise:

$$P(\text{Manifestation}|\text{EQK}: L, G, M_w) = \int_{IM} P(\text{Manifestation}|IM, M_w) f(IM|L, G, M_w) \cdot dIM \quad (3)$$

$$P(\text{No Manifestation}|\text{EQK}: L, G, M_w) = 1 - \int_{IM} P(\text{Manifestation}|IM, M_w) f(IM|L, G, M_w) \cdot dIM \quad (4)$$

In these equations, uncertainty is not assigned to the observed liquefaction response; $f(IM|L, G, M_w)$ has the same meaning as above; and $P(\text{Manifestation}|IM, M_w)$ is computed by a probabilistic model that predicts the triggering of liquefaction at depth and its subsequent manifestation at the ground surface using subsurface geotechnical data. Ultimately, the uncertainties that are, and are not, accounted for in this work will be explicitly discussed.

Application of this method is demonstrated conceptually in Figure 4 considering four MMI observations and two hypothetical sources for the earthquake that produced the observations. In actual analyses, a very large number of sources is considered. Figure 5 illustrates how the relative likelihoods of these two sources are assessed. Shown in Figure 5a are the computed probabilities of individual observations, given a rupture of source one, as computed by Eq. 2 for varying M_w . In Figure 5b, this is repeated considering a rupture of source two. In Figure 5c, the likelihood of each source is computed as a function of M_w by Eq. 1 (i.e., the product of the four probability distributions in Figure 5a or 5b). In this simple example, source one has a far greater peak likelihood of producing the set of field observations, whereas source two is very unlikely to do so, regardless of its M_w . By repeating this process for an array of hypothetical sources and generating a likelihood distribution for each, the characteristics of the causative rupture (e.g., location, orientation, magnitude) are probabilistically constrained, to the degree that evidence permits. In this work, we compute M_w probability-distributions conditioned on both the hypothesized Woodstock fault and on an unknown source. The latter is accomplished by aggregating probability distributions from all hypothetical sources and thus includes the uncertainties of fault location and geometry, whereas the former assumes the fault location and geometry are known.

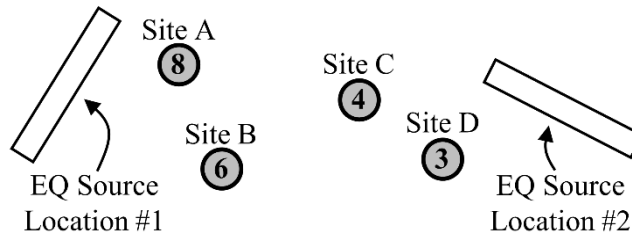


Figure 4. Hypothetical MMI inverse analysis consisting of four field sites, where MMI values were reported for each of the site locations (the value in the circle). In addition, two hypothetical sources for the earthquake that produced these observations are shown.

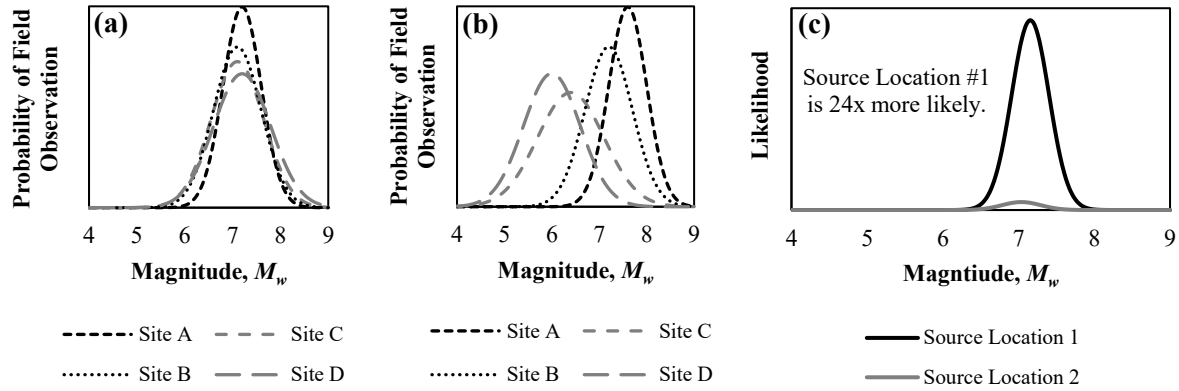


Figure 5. Approach for computing the likelihood of the sources depicted in Figure 4: (a) probabilities of individual observations, given an earthquake at location one of variable M_w ; (b) probabilities of individual observations, given an earthquake at location two of variable M_w ; (c) M_w -likelihood distributions for source locations one and two.

4.2 Implementation Details

The implementation of Eqs. 1-4 is next described in detail. This includes both general methods transferrable to other regions and to other forms of evidence, as well as the specific models adopted for the 1886 earthquake. Because the analyses of MMI and liquefaction data are procedurally similar, we first fully describe the former and then succinctly discuss differences specific to the latter. For completeness, however, the liquefaction analysis procedure is fully replicated in the electronic supplement.

As detailed in the following, two approaches will be used to model hypothetical seismic sources. These sources are first treated as earthquake epicenters on a grid pattern, which we term the “epicenter search”. To use modern GMMs, which are applicable only to faults, each epicenter is converted to an amorphous fault realization using site-to-source distance correlations, which implicitly assume some fault geometry as a function of magnitude. With this approach, the source location may be investigated (i.e., probabilistically constrained) without consideration of rupture geometry. While this reduces computational expense, it considers only a “median” geometry and thus omits one source of uncertainty. Accordingly, and following constraint of the epicentral region, seismic sources are next treated as faults having an array of locations, lengths, and orientations, which we term the “fault search.” Of these enumerable faults, one is the hypothesized Woodstock Fault, which we highlight in the results for obvious reasons.

4.2.1 MMI Analysis Procedure

The analysis of MMI data is completed via the following 15 steps:

- (1) Create an array of seismic sources. In this paper, a 62,500 km² grid of surficial points was centered on Charleston. Within this grid, a finer point spacing increases spatial resolution while a coarser spacing

decreases computational demand (which can be significant, and tractable only with high performance computing). Having found that 1 km and 10 km spacing produce nearly identical outcomes, we adopted the latter spacing when studying MMI observations. These surficial points will be treated first as earthquake epicenters (i.e., the “epicenter search”) and second as surface projections of the centroids of faults (i.e., the “fault search”).

(2) Select N study sites (i.e., the *MMI* observations compiled by Bakun et al. (2002)).

(3) Select an appropriate GMM. In this paper, the 17 GMMs developed by the NGA East Project (Goulet et al., 2018) were coalesced in a logic tree using the weights proposed by Goulet et al. (2018). Using this scheme, the least and greatest model weights were $\sim 2\%$ and 10% , respectively.

(4) For each seismic source created in (1):

(5) For each seismic-source M_w considered (a range of $M_w 4$ to $M_w 8.2$ – the applicable range of the adopted GMMs – was used in this paper):

(6) For each of N study sites selected in (2), cycling from $i = 1$ to N :

(7) Compute the site-to-source distance(s) required by the GMM chosen in (3), as measured from study site i to the seismic source selected in (4). For the GMMs adopted herein, the only such metric required is-the closest distance to fault rupture (R_{RUP}). When the seismic sources in (1) are treated as epicenters, rather than faults, the correlations of Scherbaum et al. (2004) were used to estimate a median R_{RUP} from epicentral distance (R_{EPI}). In effect, these correlations, which are magnitude dependent, convert each epicenter from (1) into a median realization of a multidimensional fault. Alternative approaches to estimating R_{RUP} from point sources are provided by Bommer et al. (2016) and Thompson and Worden (2018). Ultimately, the sources in (1) are explicitly modeled as faults to determine whether the field evidence can constrain the 1886 source beyond a point location. In doing so, R_{RUP} is directly measured from fault planes and the uncertainty of fault orientation is considered.

(8) Using the GMM in (3), M_w from (5), and site-to-source distances from (7), compute the probability density function (PDF) of expected *PGA* at site i , modified for site effects. In general, this PDF is a lognormal random variable described by a median and lognormal standard deviation, which are given by a GMM. *PGA* predictions beyond ± 3 standard deviations of the median were truncated, as is typical, and the PDF was scaled such that the area beneath it was one. In this study, the ENA weighted GMM predicts *PGA* for reference rock conditions. Accordingly, the V_{S30} -dependent model of Harmon et al. (2019), which is ENA-specific and developed as part of the NGA-East Project, was used to adjust *PGAs* for local site effects. V_{S30} was estimated at the site of each field observation using the Heath et al. (2020) maps.

(9) For each possible *PGA* value at study site i , as computed in (8) for a given M_w and R_{RUP} pair:

(10) Select an IM-MMI model. In this paper, the Atkinson and Kaka (2007), Worden et al. (2012), Caprio et al. (2015), and Cramer (2020) models were adopted. The inputs to these models vary but generally include

381 PGA , M_w , and R_{RUP} . The median MMI predicted by each model is plotted in Figure 6 as a function of
 382 PGA considering an $M_w 6$ event at $R_{RUP} = 100$ km.

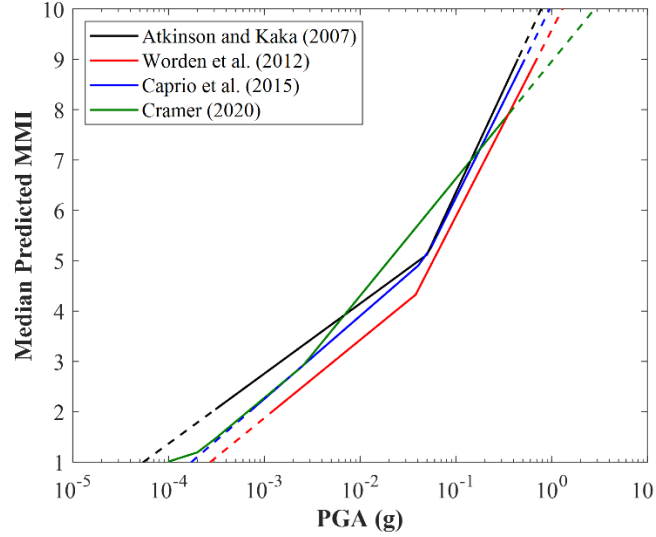


Figure 6. Predicted median MMI versus PGA according to four recent models (where applicable, $M_w = 6.0$; $R_{RUP} = 100$ km). Solid lines indicate the range of each model's proposed applicability (typically the range of training data); dashed lines indicate extrapolation beyond these respective bounds.

- 383 (11) Using the IM-MMI model selected in (10), the R_{RUP} from (7), and the PGA from (9), compute the PDF
 384 of expected MMI at study site i . In this paper, MMI predictions beyond $1 \leq MMI \leq 10$ were truncated
 385 because the definition of MMI gives a lower bound of 1 and because intensities greater than 10 are rarely
 386 assigned in practice (Stover and Coffman, 1993). Following truncation (when applicable) the PDF was
 387 scaled such that the area underneath it was one.
- 388 (12) For each possible MMI value at study site i , as computed in (11):
- 389 (13) Compute the probability of field observation as described in Eq. 2. Completing this equation (i.e., by
 390 multiplying the probability of field observation by the probabilities of MMI and PGA , then summing over
 391 all MMI and PGA values) gives the probability of the field observation at site i for a given seismic source
 392 location, geometry, and M_w . Repeating steps 6-13 for all M_w results in a probability of field observation
 393 curve for each source, examples of which are in Figures 5a and 5b.
- 394 (14) Compute the likelihood of a seismic source (as evidenced by MMI) as a function of M_w by multiplying
 395 the probabilities of all field observations (i.e., multiply the curves in Figures 5a or 5b at each value of
 396 M_w). The result, an example of which is shown in Figure 5c, is a likelihood distribution of M_w conditioned
 397 on a single seismic source (i.e., assuming that a fault with given location and geometry, but unknown M_w ,
 398 is responsible for producing the field observations).

399 (15) Repeating steps 5-14 for all seismic sources created in (1) results in a likelihood distribution of M_w for
400 each. Collectively, this field of distributions describes the locations and magnitudes of earthquakes that
401 are, and are not, likely to produce the field evidence. To allow for relative likelihoods to be compared
402 visually, we normalize the likelihood of each source by the peak likelihood among all sources, such that
403 the most likely source has a normalized peak value of one. We then map contours of likelihood to identify
404 this location. The M_w distribution at this location (see Figure 5c) is the PDF of the inverted M_w conditioned
405 on the most likely source. Finally, by aggregating PDFs from all potential sources in (1), an overall PDF
406 of M_w , considering all possible sources, is produced. While a single source will always be “most likely,”
407 earthquakes at other locations typically also have potential to produce the evidence. This latter PDF,
408 conditioned on all possible sources, includes that uncertainty.

409 4.2.2 Liquefaction Analysis Procedure

410 The analysis of liquefaction is akin to that of MMI, differing only in steps (10) through (13) of the
411 preceding. Once site-adjusted $PGAs$ are predicted at sites of observation (in this case, sites with liquefaction
412 observations), the factor of safety against liquefaction is computed throughout the soil profile using the
413 Boulanger and Idriss (2014) CPT-based triggering model, which is a function of PGA , M_w , and subsurface
414 geotechnical data. As part of this procedure, the effects of soil aging are separately accounted for with three
415 proposed models, in addition to a control analysis without any such accounting. Two of these models,
416 henceforth termed “A” and “B”, are regional-scale corrections based on the Weems et al. (2014) geology
417 map of the Charleston region, whereas Model “C” uses site-specific measurements. Model A uses the
418 Hayati and Andrus (2009) aging-correction model based on the measured to estimated shear-wave velocity
419 ratio (MEVR). As MEVR increases, the shear stiffness of soil measured at small strain exceeds that inferred
420 from large strain measurements, which may be interpreted as an indicator of cementation. Median MEVR
421 values for each geologic unit were adopted from the regional sampling of Heidari and Andrus (2012). Model
422 B uses the Hayati and Andrus (2009) correction model based on depositional age, which we estimated for
423 each geologic unit from the Weems et al. (2014) map. As a deposit’s age increases, an increasingly larger
424 correction is applied to the computed liquefaction resistance. Lastly, Model “C” again adopts the MEVR-
425 based approach of Hayati and Andrus (2009), but in this case MEVR is directly computed at each study
426 site using data from seismic CPTs (i.e., CPT resistances and shear-wave travel times) per the method of
427 Andrus et al. (2009). This approach produced corrections that tended to exceed those of Models A and B.
428 While corrections from Model C – being based on site-specific subsurface data – should be most efficient,
429 all such corrections are likely very uncertain and the best approach to account for soil aging is actively
430 debated. We thus argue that all three models, which scale upward the computed liquefaction triggering
431 resistance at depth, warrant consideration. However, given that the field observations are of surface

manifestations (i.e., liquefaction vents and dikes) rather than observations of liquefaction at discrete depths, surface manifestations must be predicted for proper comparison to field observations. Accordingly, the liquefaction potential index (*LPI*) of Iwasaki et al. (1978) was adopted, given its longstanding use:

$$LPI = \int_0^{20m} F(FS_{liq}) \times w(z) dz \quad (5)$$

where $F(FS_{liq})$ and $w(z)$ weight the respective influences of FS_{liq} and depth, z , on surface manifestation. In brief, *LPI* assumes that manifestation depends on the FS_{liq} in each soil stratum, the thickness of all liquefied strata, and the proximity of those strata to the surface. Given this definition, *LPI* can range from 0 to 100. Next, the probability of liquefaction manifestation was computed at each study site, considering all values of M_w from (5) and all values of PGA from (9), using the fragility function of Geyin and Maurer (2020), which relates the probability of liquefaction manifestation to *LPI*, and which was trained on all globally available CPT-based liquefaction case histories. Lastly, and analogous to (13), the probability of what was observed in the field was computed by Eq. 3 or 4, depending on whether manifestations were or were not observed. The liquefaction analysis procedure is fully replicated in the electronic supplement.

5. Results and discussion

Using the above data and methodologies, the source of the 1886 Charleston rupture was rigorously investigated. Results are separately presented for MMI and liquefaction evidence. For each, three types of analyses were performed, namely the: (i) “epicenter search”, wherein seismic sources were modeled as points; (ii) “fault search,” wherein seismic sources were modeled as faults; and (iii) “Woodstock Fault,” wherein the hypothesized Woodstock Fault is directly considered. The first provides preliminary probability distributions of the source location and magnitude. The second provides final distributions that include additional source-model uncertainties and conveys whether the orientation of the causative fault can be constrained. The third provides results conditioned on the singular Woodstock Fault and should be adopted if all other seismic sources, known and unknown, are dismissed as sources of the 1886 earthquake.

5.1 Analysis of MMI Data: Epicenter Search (Seismic Sources Modelled as Points)

Treating seismic sources as points, the inversion methodology was applied using the Atkinson and Kaka (2007), Worden et al. (2012), Caprio et al. (2015), and Cramer (2020) IM-MMI models. For brevity, these models are henceforth titled AK07, WEA12, CEA15, and C20. For these analyses, MMI observations were studied if within 600 km of Charleston. While the sensitivity of this decision will be analyzed further, it was made based on a trait of the Bakun et al. (2002) MMI dataset that we view as problematic, but which prior researchers have not discussed. Namely, Bakun et al. (2002) did not include “negative” observations (i.e., MMI values of 1 or 2) where ground motions were not perceived. This is notable, given that a

distribution of MMI values is naturally experienced at any given distance. Problematically, the omission of low MMI values asymmetrically truncates this distribution at large distances (i.e., those where some observers report MMI 1 or 2). The analysis of this dataset at large distances thus potentially has the effect of biasing inverted magnitudes toward larger values, since those magnitudes need not adhere to small MMI values that were experienced, but which were systematically undocumented. The analysis of data only at small distances is equally undesirable, of course, given the inherent benefits of analyzing more data over a wider spectrum of attenuation. Based on these competing interests and given that we begin to observe evidence of MMI truncation at distances exceeding 600 km, this threshold was provisionally selected.

The resulting geospatial contours of seismic-source likelihood are shown in Figure 7 for the WEA12 model. Also shown is the surface projection of the hypothesized Woodstock fault (Durá-Gómez and Talwani, 2009a,b), as well as historical epicenters ($M_w > 1.0$; 1900-present). These contours show the source locations most and least likely to produce the MMI evidence. Using the WEA12 model, a zone of high likelihood is computed just northwest of the Woodstock Fault projection, with the most likely source located 2 km from the mapped projection. By contrast, source locations to the south and east are comparatively very unlikely to produce the MMI observations. For brevity, results using the AK07, CEA15, and C20 models are summarized in Figure 7 via stars, which denote the epicenters deemed most likely by each model. Complete contour maps, analogous to those in Figure 7 for WEA12, are provided in the electronic supplement. While CEA15 produces a result similar to WEA12, with the most likely source inside the Woodstock Fault projection, AK07 and C20 suggest most likely sources ~10 km and ~35 km east of the projection. Thus, all analyses point to a source north of Charleston. Some IM-MMI models strongly support an earthquake source in the immediate vicinity of the hypothesized Woodstock Fault, while others do not.

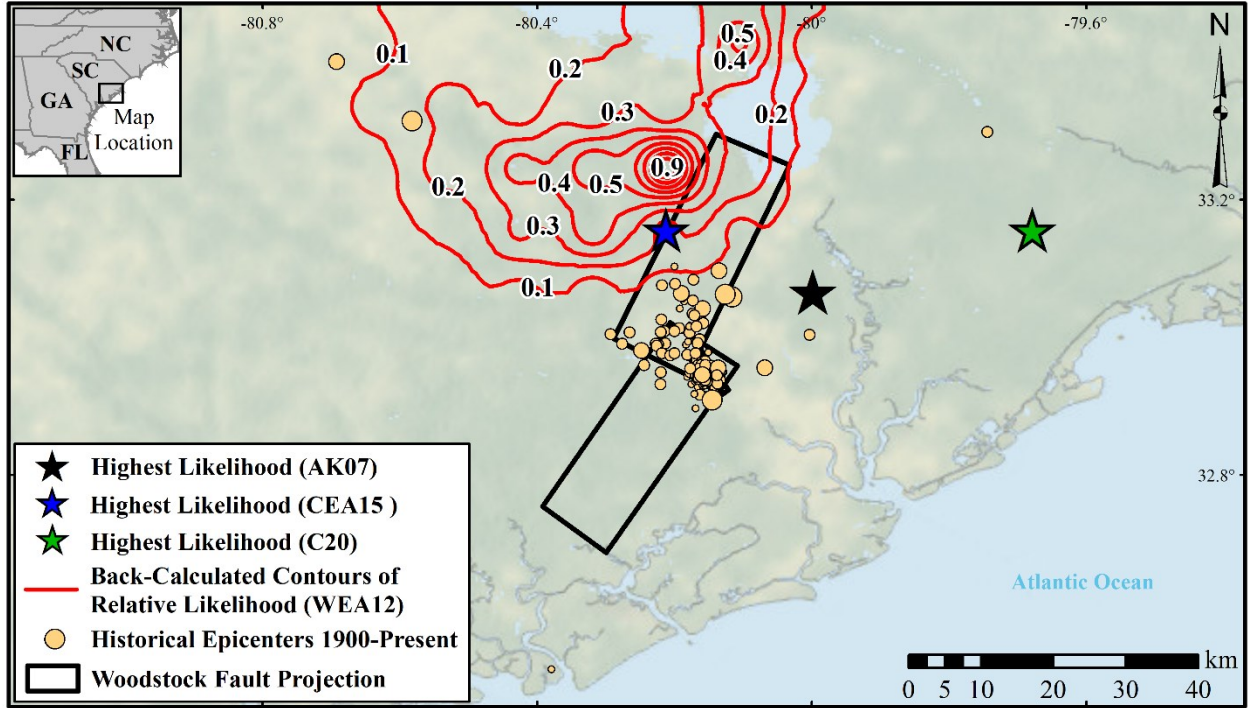


Figure 7. Likelihood contours produced using the WEA12 model which indicate source locations that are, and are not, likely of producing the MMI evidence. Stars = the most likely source locations per the AK07, CEA15, and C20 models; AK07 = Atkinson and Kaka (2007), WEA12 = Worden et al. (2012), CEA15 = Caprio et al. (2015), C20 = Cramer (2020); black rectangles = the Woodstock fault projection (Durá-Gómez and Talwani 2009a,b); tan circles = historical epicenters ($M_w > 1.0$; 1900-present) (USGS, 2022).

Shown in Figure 8 are the cumulative distribution functions (CDFs) of M_w inverted from MMI data, as computed with each of the four IM-MMI models. These results include the uncertainty of an unknown source (epicenter) location, the uncertainties of expected shaking intensities conditioned on a given source, considering also the epistemic uncertainty of GMM selection, and the uncertainties of the IM-MMI models. For comparison, the CDF assigned to the Charleston source in the NSHMP (Petersen et al., 2014, 2020) is also shown and ranges from $M_w 6.7$ to $M_w 7.5$ with a median of $M_w 7.1$. AK07 and C20 produce nearly identical CDFs with a median of $M_w 7.1$. WEA12 and CEA15 produce similarly identical CDFs, but with a median of $M_w 7.3$. The grouping of these outcomes can be traced to Figure 6. AK07 and C20 tend to predict larger MMIs for a given PGA. As a result, smaller magnitude ruptures result from the use of AK07 and C20 within the inversion methodology. Each of the individual CDFs has relatively low uncertainty. This can be attributed to: (i) the large quantity of MMI observations; (ii) the fact that not all uncertainties are considered (e.g., those of site conditions or rupture geometry, among others); and (iii) the relatively large variance of MMI observations over any given site-to-source distance. Regarding the last, extreme outliers from the mean MMI trend have the effect of yielding very low likelihoods for small and large magnitude

events. That is, only a narrow range of magnitudes are likely to simultaneously produce MMI observations of, say, 3, 5, and 7 at the same site-to-source distance and on similar site profiles. Conversely, a wider range of magnitudes could simultaneously produce MMI observations of 4, 5, and 6. While geostatistical analyses could conceivably identify and delete observations that are extreme outliers, the justification would be largely speculative without an intensive reinvestigation. In other words, we are unaware of any objective basis for deleting some MMI reports but not others in the absence of a complete reinterpretation of the more than 1000 original intensity reports. Lastly, to include the epistemic uncertainty of IM-MMI model selection, each CDF was weighted to produce an ensemble CDF, as shown in Figure 8. This selection of weights is heuristic, as no quantitative justification could be identified (e.g., based on model residuals in ENA). The weights and justifications are as follows. C20 (0.4) is the latest ENA-specific model and was trained using the largest quantity of ENA data. AK07 (0.3) is also ENA-specific, but also found no need for region-specific models within North America. For that reason, and because differences in methodology (e.g., data selection, intensity scales, regression techniques) can result in very different models with apparently similar performance (i.e., on the respective training sets), we hesitate to omit other reputable models even if nonspecific to ENA. Accordingly, WEA12 (0.15), which was trained only on California data, and CEA15 (0.15), which was trained on global data including some from ENA, are also weighted in the ensemble. While CEA15 might otherwise warrant greater weighting, its training set was truncated at a site-to-source distance of 200 km, which calls into question its suitability in ENA, where ground motions are commonly felt at greater distances (as in the 1886 event).

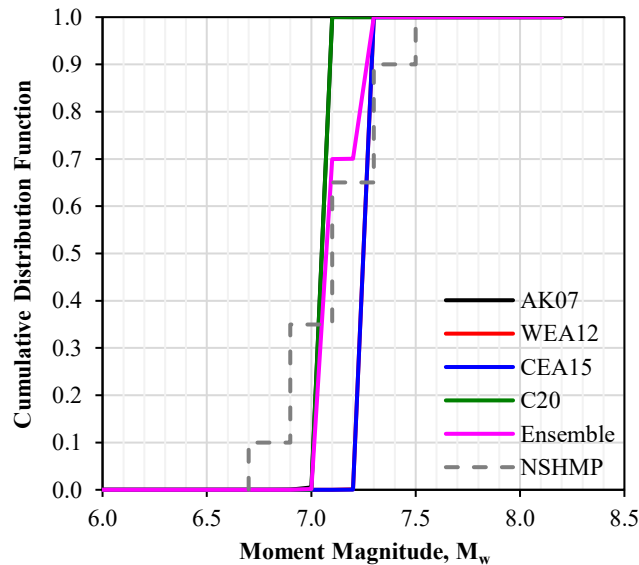


Figure 8. CDFs of rupture magnitude, as inverted from MMI observations using four IM-MMI models, wherein seismic sources are modelled as points. AK07 = Atkinson and Kaka (2007), WEA12 = Worden et al. (2012), CEA15 = Caprio et al. (2015), C20 = Cramer (2020), and NSHMP = National Seismic Hazard Model Project (Petersen et al., 2014, 2020).

5.2 Analysis of MMI Data: Fault Search (*Seismic Sources Modelled as Faults*)

To determine whether MMI observations can constrain the seismic source beyond a point location, the point sources were next treated as surface projections of the centroids of faults. For simplicity, the faults were initially assumed to be strike-slip with a dip of 90 degrees. The orientations of the faults were discretized into strike azimuths of 30° increments (i.e., 0°, 30°, 60°...). The lengths of the faults were computed via the magnitude-dependent correlation of Wells and Coppersmith (1994). The depth to the top of rupture was estimated using the correlation of Kaklamanos et al. (2011), which produces estimates consistent with the inferred depths of modern ruptures in the region (Chapman et al., 2016). Thus, while not every aspect of rupture geometry was assigned uncertainty, the analyses can nonetheless determine whether some fault alignments (e.g., the hypothesized Woodstock Fault) are more likely than others to produce the observed evidence. With this approach, the inversion methodology was again applied to the Bakun et al. (2002) dataset using each of the four IM-MMI models.

Results are shown in Figure 9 for the WEA12 model in the style of a heat map. Faults more likely to produce the MMI observations have thicker lineweight and are darker in color. Faults very unlikely to produce the evidence have thin lineweight and light color, and thus blend with the map's background. Also shown is the surface projection of the hypothesized Woodstock Fault (Durá-Gómez and Talwani 2009a,b) as well as historical epicenters. While most modelled faults are relatively unlikely to produce the evidence, the faults deemed most likely align with the hypothesized Woodstock Fault, albeit their magnitudes are greater than most prior estimates. The singular fault most likely to produce the MMI evidence, for example, has a median M_w of 7.60. Faults striking E-W and N-S have lesser, but nontrivial, likelihoods of producing the MMI evidence.

For brevity, results using the AK07, CEA15, and C20 models are each summarized in Figure 9 by single lines, which denote the singular faults deemed most likely by each model. Complete heat maps, analogous to those in Figure 9 for WEA12, are provided in the electronic supplement. These three models produce results that are similar to one another and different from WEA12, with the most likely faults oriented perpendicular to the Woodstock Fault and located partly offshore. These most-likely faults range in median magnitude from M_w 7.20 to M_w 7.90. A close inspection of these results (electronic supplement) reveals that each of these models finds faults consistent with the Woodstock Fault to have low relative likelihoods of producing the MMI evidence, as compared to all other hypothetical faults. It is worth noting that the two ENA-specific IM-MMI models (AK07 and C20) point to faults inconsistent with the Woodstock Fault. While these results do not necessarily indicate that the Woodstock Fault was not responsible for the 1886 earthquake, they do indicate that the causative fault cannot currently be constrained by the available MMI evidence. That is, faults striking SE and partly offshore are just as likely to produce this evidence as faults striking NE and onshore. While different assumptions about fault depth, length, and

dip invariably change the results, a parametric analysis indicates that these changes are minor, upholding the overall conclusion that the MMI data cannot constrain the 1886 fault rupture. If anything, the data point to a fault striking SE and partly offshore. This conclusion might be different if: (i) more MMI observations were available in the near field; and (ii) the affected area was not on a coastline. Analogous to the inversion of an epicenter from wave-arrival times, which relies on distributed instruments, this inversion relies on distributed observers to “record” the amplitudes of ground motions. Thus, in events such as this, where the near-field is not more densely populated with observations than the far field, and where observations are geographically asymmetric, it may be more difficult to detect directions and rates of ground-motion attenuation, and thus more difficult to constrain the causative fault from which motions propagated.

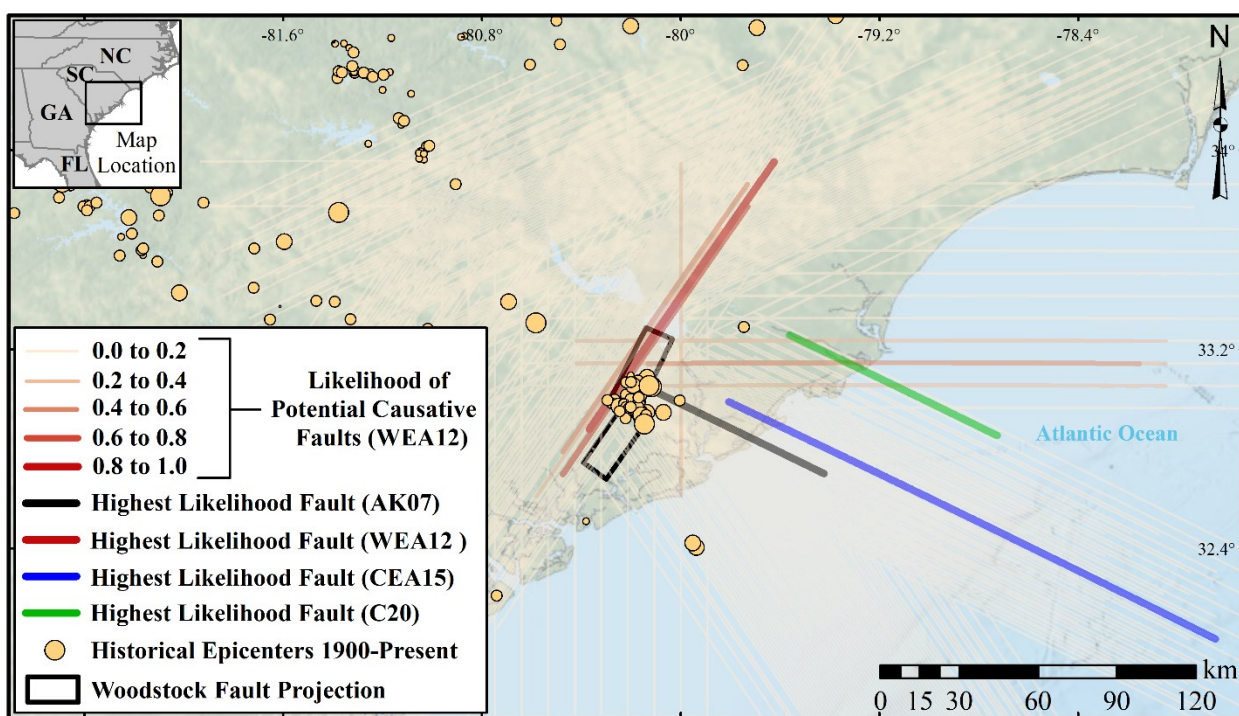


Figure 9. Likelihoods of hypothetical faults with differing orientations and lengths to produce the MMI evidence, as obtained using the WEA12 model. Also shown are the singular faults deemed most likely using the AK07, CEA15, and C20 models; AK07 = Atkinson and Kaka (2007), WEA12 = Worden et al. (2012), CEA15 = Caprio et al. (2015), C20 = Cramer (2020); black rectangles = the Woodstock projection (Durá-Gómez and Talwani 2009a,b); tan circles = historical epicenters ($M_w > 1.0$; 1900-present) (USGS, 2022).

Shown in Figure 10 are the CDFs of M_w inverted from MMI data via the “fault search”, as computed with each of the four IM-MMI models. These results include the uncertainty of an unknown source location, the uncertainty of unknown fault orientation, the uncertainties of expected shaking intensities conditioned on a given source and considering the epistemic uncertainty of GMM selection, and the uncertainties of the

IM-MMI models. It should be emphasized that these results do not include every source of uncertainty. Omitted, for example, are the uncertainties of: (i) fault depth and length; (ii) fault dip; and (iii) site V_{S30} . For each of these inputs only a median prediction was used. For comparison, the CDF assigned to the Charleston source in the NSHMP (Petersen et al., 2014, 2020) is also shown. Like the “epicenter search” results in Figure 8, the AK07 and C20 models produce similar CDFs with a lesser median of $\sim M_w 7.2$, while WEA12 and CEA15 produce similar CDFs with a greater median of $\sim M_w 7.7$. It is readily apparent that the epistemic uncertainty of IM-MMI model selection is considerable. To account for this uncertainty, each CDF was weighted per the prior scheme to produce an ensemble CDF, as shown in Figure 10, which has a median of $\sim M_w 7.25$ and 95% CI of $M_w 7.05$ to $M_w 7.85$. In this regard, efforts to better quantify the suitability of various IM-MMI models to ENA, and in turn to refine the weighting scheme used herein, could have significant influence on the overall conclusions of this study (and presumably also on studies of other seismic sources). Despite this ambiguity, the ensemble CDF in Figure 10 suggests that ruptures larger than $M_w 7.5$ – the largest value considered in the NSHMP – could produce the observed evidence.

Of course, it should also be emphasized that the numerous hypothetical faults considered in our methodology and aggregated to form the results in Figure 10 may not exist. That is, some of these gridded faults are more likely to produce the 1886 MMI data than the hypothesized Woodstock Fault, but these various faults are not necessarily present. Conversely, there is evidence (e.g., seismological data, geophysical surveys) supporting the Woodstock Fault’s existence (Durá-Gómez and Talwani 2009a,b; Chapman et al., 2016). Accordingly, the preceding analyses are next repeated, conditioned solely on the Woodstock Fault, thereby removing all source uncertainties aside from magnitude.

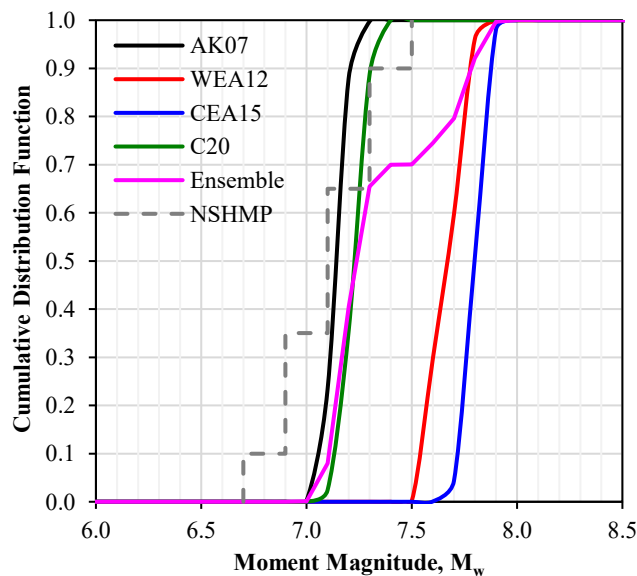


Figure 10. CDFs of rupture magnitude, as inverted from MMI observations using four IM-MMI models, wherein seismic sources are modelled as faults. AK07 = Atkinson and Kaka (2007), WEA12 = Worden et

al. (2012), CEA15 = Caprio et al. (2015), C20 = Cramer (2020), and NSHMP = National Seismic Hazard Model Project (Petersen et al., 2014, 2020).

5.3 Analysis of MMI Data: Woodstock Fault

While the parameters of the Woodstock Fault are uncertain, we adopt the source model of Durá-Gómez and Talwani (2009a,b) exactly as proposed therein, the surface projection of which appears in Figures 1, 7, and 9. While Chapman et al. (2016) do not identify the Woodstock Fault by name, they infer and describe from more recent seismological records a source that is very similar: “We interpret ...that the modern seismicity is the lingering aftershock sequence of the 1886 shock and that the mainshock occurred on a south-striking, west-dipping fault plane ...” To evaluate the prior site-to-source distance threshold of 600 km (i.e., that which was used to exclude MMI observations), these analyses were also repeated using MMI data at different site-to-source distances. Shown in Figure 11, for example, are the CDFs of M_w conditioned on the Woodstock Fault and inverted from MMI data in two distance bins: (a) < 600 km; and (b) < 400 km. Several observations are made from Figure 11 as follows.

First, it is observed that the ensemble CDF in Figure 11a is only marginally less uncertain than the ensemble CDF in Figure 10, meaning that conditioning the analysis on the Woodstock Fault does not significantly alter the results. In other words, the uncertainties of fault location and geometry are relatively minor, given the data available for analysis. As previously discussed in Figure 9, these data are unable to constrain the causative fault. That is, faults with diverse locations and orientations have similar likelihoods of producing the MMI evidence, which may be due to a paucity of near-field observations. However, because similar rupture magnitudes are inferred for these various faults irrespective of their positions, the CDFs conditioned on the Woodstock Fault and the CDFs conditioned on an unknown fault are similar.

Second, a site-to-source distance bias is observed from Figures 11a and 11b. While the CDFs become more vertical as more observations are included (reflecting a decrease in uncertainty) the CDFs also tend to increase in magnitude. Observations at distances up to 600 km suggest larger rupture magnitudes than those at distances up to 400 km. The median magnitude, for example, increases by $\sim 0.25M_w$ according to CEA15, by $\sim 0.1M_w$ according AK07 and C20, and by $\sim 0.01M_w$ according to WEA12. It could be shown that the prior “epicenter search” and “fault search” results have a similar degree of sensitivity. This distance bias could be present in either: (i) one or more of the component models utilized (e.g., the GMMs, site-response model, or IM-MMI models); or (ii) in the MMI data itself. With respect to the adopted models, all were shown to be unbiased during their respective trainings and cannot be further tested in the absence of additional data. It is worth noting again, however, that the CEA15 model, which exhibits the greatest site-to-source distance sensitivity in Figure 11, is herein applied to data much more distant than it was trained on. It was for this reason that CEA15 was given low weighting despite having a large global training set. With respect to the MMI data, we reiterate that analyzing more data over a wider spectrum of attenuation

is beneficial but remain adamant that the Bakun et al. (2002) dataset is apt to introduce bias at large distances, given that small MMI values were systematically undocumented. To further probe the issue of IM-MMI model applicability, the analyses were performed using only the data to which each model is applicable (as stated by the original authors, or otherwise interpreted by the present authors). Specifically, the WEA12, AK07, CEA15, and C20 models were respectively applied to observations within site-to-source distances of 400 km, 800 km, 200 km, and 1500 km. The results are shown in Figure 11c. The most salient changes are: (i) the CEA15 CDF is more uncertain (due to fewer field observations) and has a reduced median of $\sim M_w 7.2$; and (ii) the C20 CDF is less uncertain (due to more field observations) and has an increased median of $\sim M_w 7.35$. In summary, we are unsure why the results show evidence of site-to-source distance bias at distances less than 600 km. However, we argue that the bias observed at larger distances (e.g., the C20 result in Figure 11c) is at least partly due to the aforementioned bias of the Bakun et al. (2002) dataset. As such, we prefer not to glean new conclusions from Figure 11c or champion its results over those in Figure 11a. Our preferred CDF conditioned on the Woodstock Fault thus has a median of $M_w 7.10$ and 95% CI of $M_w 7.0$ to $M_w 7.75$. Given an unknown source, our preferred CDF (Figure 10) has median of $\sim M_w 7.25$ and 95% CI of $M_w 7.05$ to $M_w 7.85$. For either result, the epistemic uncertainty of IM-MMI model selection has significant influence.

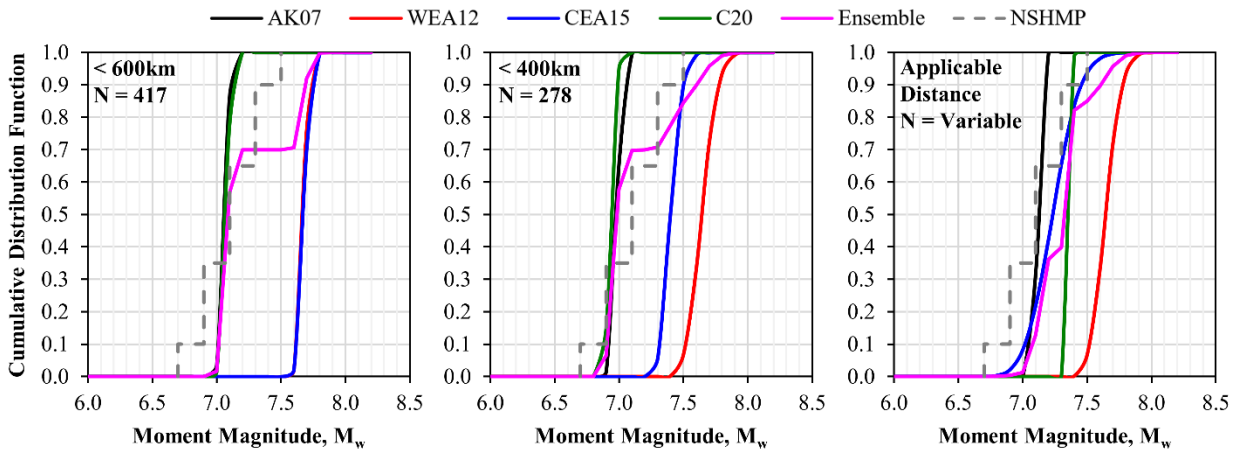


Figure 11. CDFs of rupture magnitude, as inverted from MMI observations using four IM-MMI models and assuming the Woodstock Fault (Durá-Gómez and Talwani, 2009a,b) to be the earthquake source. AK07 = Atkinson and Kaka (2007), WEA12 = Worden et al. (2012), CEA15 = Caprio et al. (2015), C20 = Cramer (2020); NSHMP = National Seismic Hazard Model Project (Petersen et al., 2014, 2020).

5.4 Analysis of Liquefaction Data: Epicenter Search (Seismic Sources Modelled as Points)

The inversion methodology was next applied to the 24 study sites summarized in Table 2 where the 1886 liquefaction response was observed, or has since been investigated, and where CPT testing has been performed. Analogous to the analysis of MMI data, the seismic source was first treated as an epicenter with

unknown location. The resulting contours of seismic-source likelihood, which depict the epicenters most and least likely to produce the observed liquefaction response, are mapped in Figure 12, as are the 24 study sites. Also shown are historical epicenters and the hypothesized Woodstock Fault (Durá-Gómez and Talwani, 2009a,b). These initial results include no correction to account for the effects of soil aging on liquefaction. As shown in Figure 12, the analysis identified a source area east of the Woodstock fault. While the single most likely epicenter is 9 km from the proposed fault projection, epicenters within the projection have up to 70% relative likelihood. Notably, these geolocation results are largely insensitive to the treatment of soil aging. Because aging correction models tend to adjust the computed liquefaction resistances by similar amounts, the inverted magnitude tends to be significantly affected, whereas the inverted, most likely source location does not. For this reason, geolocation results are not shown for each aging-correction model. All give similar results to those in Figure 12, indicating that an epicenter more than ~20 km in any direction from the northern Charleston Peninsula (e.g., the Charleston Airport) is relatively unlikely to produce the observed evidence.

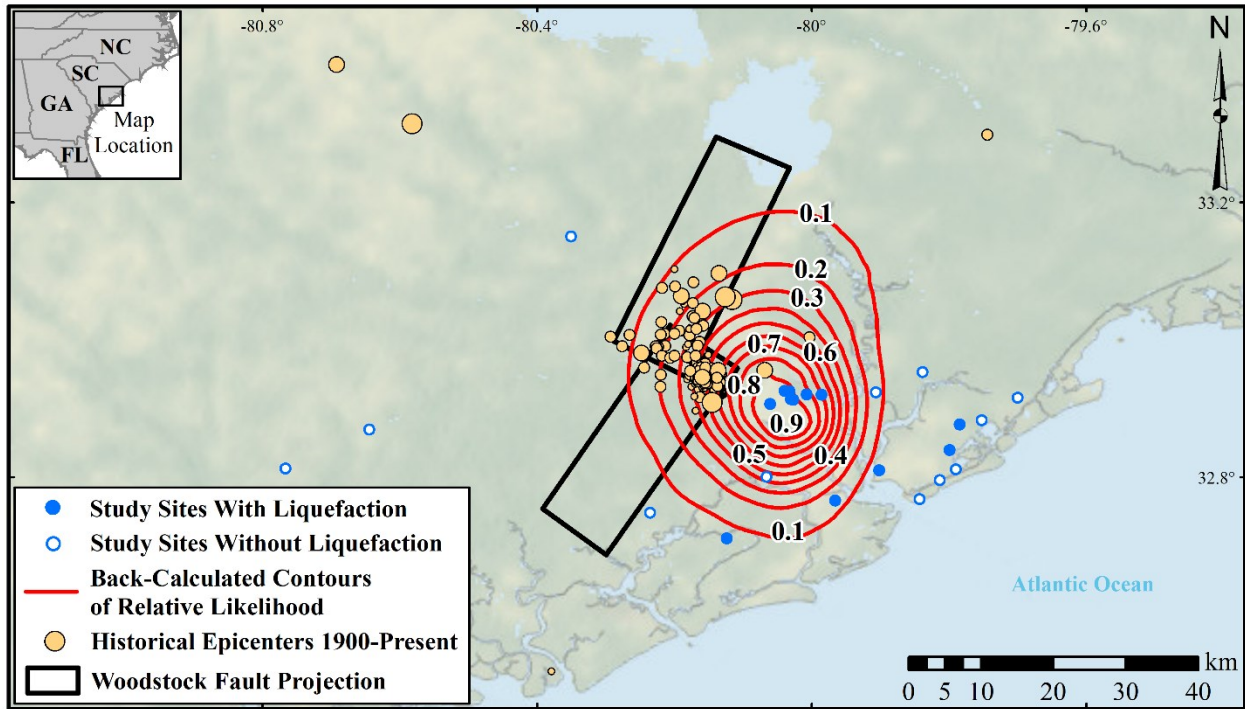


Figure 12. Likelihood contours indicating source locations that are, and are not, likely of producing the observed liquefaction response. Black rectangles = the Woodstock fault projection (Durá-Gómez and Talwani 2009a,b); tan circles = historical epicenters ($M_w > 1.0$; 1900-present) (USGS, 2022).

Shown in Figure 13 are the CDFs of M_w inverted from liquefaction evidence, as computed using: (i) no aging correction; and (ii) each of the three correction methods discussed in the *Liquefaction Analysis*

Procedure (i.e., Models “A, B, and C”). It is apparent from Figure 13 that the uncertainties of *whether* and *how* to correct for the effects of soil aging have significant influence, with the inverted median magnitudes ranging from $\sim M_w 6.3$ (no aging correction) to $\sim M_w 7.0$ (Model C). Irrespective of soil aging, it is also apparent that a magnitude inverted from the available liquefaction evidence is: (i) more uncertain than a magnitude inverted from the available MMI evidence; and (ii) more uncertain than past studies have reported. The former is attributable to there being far more MMI data than liquefaction data. The latter, as previously discussed, is attributable to published uncertainty bounds (e.g., “ $M_w 6.8$ - $M_w 7.0$ ”) being ranges of the *median* magnitude considering one source of uncertainty, which is distinctly different from a CDF of magnitude. Consequently, these results suggest more uncertainty than is adopted in the NSHMP. Magnitudes above $M_w 6.7$ and below $M_w 7.5$, for example (i.e., the limits of the NSHMP weighting), have non-trivial probabilities of producing the field evidence. It should also be noted that these results do not include uncertainty within the aging-correction models (which are certainly uncertain). That is, the models provide a median correction factor. To include the epistemic uncertainty of model selection, each CDF was weighted to produce an ensemble. As with the MMI results, our selection of weights is based more on judgement than on quantitative evidence. While we agree with the developers of aging-correction models that corrections are likely warranted, these corrections are actively debated and likely have large uncertainty. The weights selected and their justifications are as follows. Model C (0.5) is the only site-specific method. It uses detailed subsurface geotechnical measurements from each study site to compute site-specific corrections and thus arguably warrants the greatest weighting. In contrast, Models A (0.25) and B (0.25) both rely on a sampling of the median characteristics of the geologic unit in which each study site resides (e.g., the age of the unit). These models, which do not use site-specific information, are therefore better suited for regional scale analyses (i.e., where subsurface data is unavailable). Nonetheless, we argue these models warrant weighting given the overall uncertainty and debate surrounding aging corrections. The ensemble CDF has a median of $\sim M_w 6.90$ and 95% CI of $M_w 6.05$ to $M_w 7.85$.

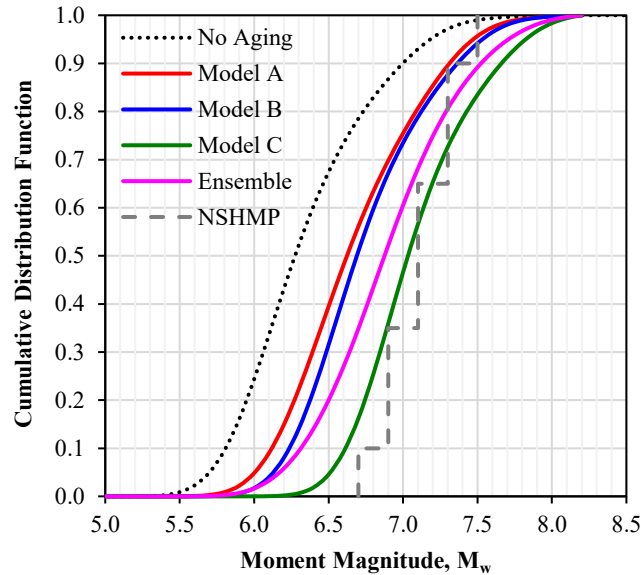


Figure 13. CDFs of rupture magnitude, as inverted from liquefaction observations using three age correction models, wherein seismic sources are modelled as points. NSHMP = National Seismic Hazard Model Project (Petersen et al., 2014, 2020).

5.5 Analysis of Liquefaction Data: Fault Search (Seismic Sources Modelled as Faults)

To determine whether the liquefaction data can constrain the seismic source beyond a point location, the epicenters were next converted to faults. The discretization and treatment of hypothetical fault sources was identical to the MMI analyses. The results without correction for soil aging are shown in Figure 14. It can be seen that the data are incapable of constraining the seismic source to the Woodstock Fault, or to any other hypothetical alignment. The faults deemed most likely to produce the field evidence strike SE (like the predominant result from MMI analysis), but faults with nearly any orientation also have high relative likelihoods. These faults all strike through the general area previously identified via the epicenter search (i.e., through the northern Charleston Peninsula). While faults striking NE do have some likelihood of producing the evidence, these faults deviate from the proposed position of the Woodstock Fault. Results using each of the aging correction models are very similar to those in Figure 14 and are therefore not presented. The use of these models increases the inverted magnitudes (and thus increases the fault lengths in Figure 14), but otherwise has little effect on the inferred fault location or orientation. As with the MMI analyses, this should not be interpreted to mean that the Woodstock Fault or any similar alignment was not the source of the 1886 earthquake. Rather, this should be interpreted to mean that many aspects of the causative fault cannot be constrained with the available macroseismic evidence. This evidence is only marginally supportive of the Woodstock Fault's existence, which is not to say it doesn't exist. This conclusion might be different if more liquefaction study sites were available to the analysis, or if the component prediction models were less uncertain.

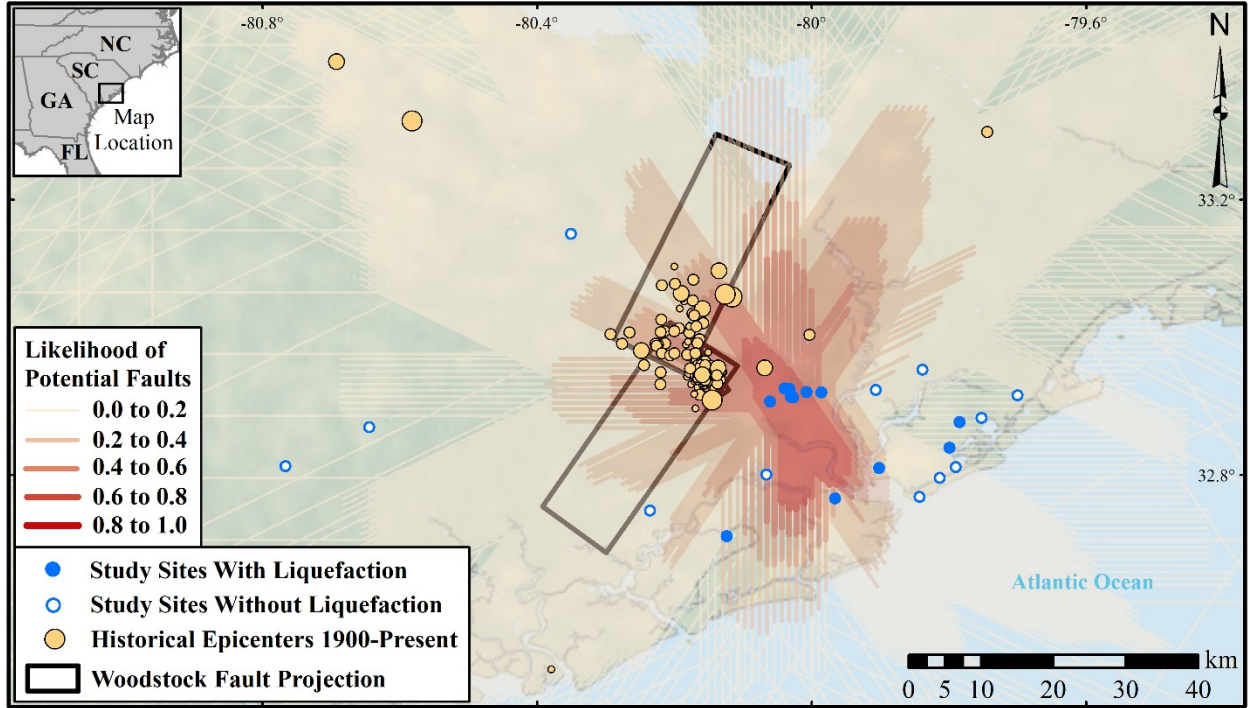


Figure 14. Likelihoods of hypothetical faults with differing orientations and lengths to produce the liquefaction evidence (no aging correction). Black rectangles = Woodstock fault projection (Durá-Gómez and Talwani 2009a,b); tan circles = historical epicenters ($M_w > 1.0$; 1900-present) (USGS, 2022).

Shown in Figure 15 are the CDFs of M_w inverted from liquefaction data via the “fault search.” The large uncertainty of a magnitude inferred from the liquefaction data is again apparent, as is the influence of soil aging and its correction. It is again emphasized that these results do not include every source of uncertainty. Omitted, for example, are the uncertainties of: (i) fault depth and length; (ii) fault dip; (iii) site V_{s30} ; and (iv) aging-correction model uncertainty. For each of these inputs only a median prediction was used. To account for the uncertainty of selecting aging-correction models, each CDF was weighted per the prior scheme to produce an ensemble CDF, as shown in Figure 15. This ensemble has a median of $M_w 6.95$ and 95% CI of $M_w 6.15$ to $M_w 7.85$, suggesting a similar median magnitude as the NSHMP (Petersen et al., 2014, 2020) but much greater uncertainty.

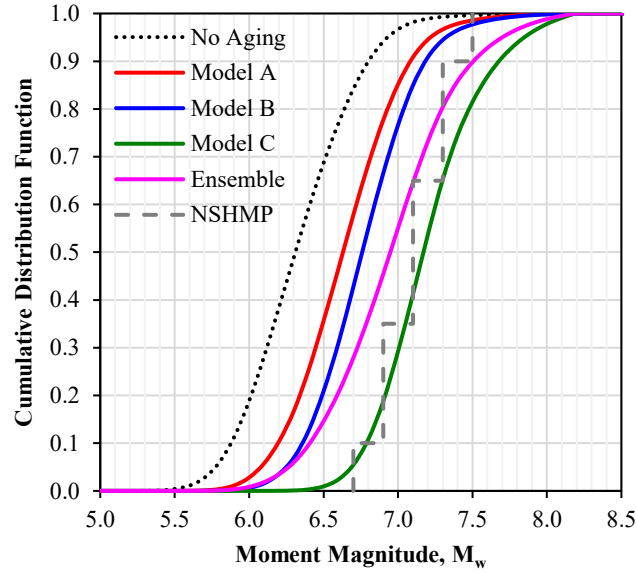


Figure 15. CDFs of rupture magnitude, as inverted from liquefaction observations using three age correction models, wherein seismic sources are modelled as faults. NSHMP = National Seismic Hazard Model Project (Petersen et al., 2014, 2020).

5.6 Analysis of Liquefaction Data: Woodstock Fault

Finally, the preceding analyses were repeated, but conditioned solely on the Woodstock Fault as hypothesized by Durá-Gómez and Talwani (2009a,b). The computed CDFs of M_w , including the weighted ensemble, are shown in Figure 16. Our preferred CDF (i.e., the ensemble) has a median of $M_w 7.20$ and 95% CI of $M_w 6.30$ to $M_w 8.10$. Relative to the CDF conditioned on an unknown source in Figure 15, conditioning on the Woodstock Fault increases the inverted magnitude by $\sim 0.2 M_w$ and increases the M_w uncertainty. This counterintuitive increase in uncertainty is attributable to the epistemic uncertainty of selecting aging-correction models, which is observed to increase with increasing rupture magnitude. Because conditioning on the Woodstock Fault increases the inverted rupture magnitude, differences between the aging-correction models become more apparent. Nonetheless, and similar to the analysis of MMI data, the uncertainties of fault location and geometry appear relatively minor compared to other uncertainties, given the data available for analysis. As shown in Figure 14, faults with diverse orientations were found to have similar likelihoods of producing the liquefaction evidence. In other words, the data are sufficient to constrain the source to a general area but are insufficient to constrain the source to a specific fault alignment. However, because similar magnitudes are inferred for these faults irrespective of their positions, the CDFs conditioned on the Woodstock Fault and the CDFs conditioned on an unknown source are similar.

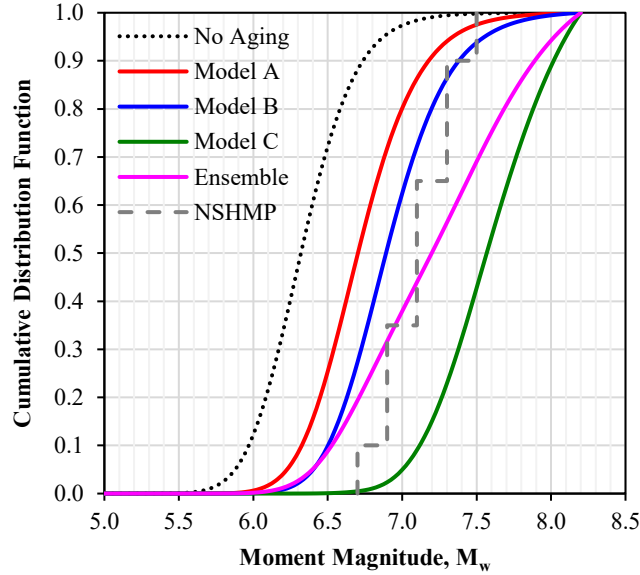


Figure 16. CDFs of rupture magnitude, as inverted from liquefaction observations using three age correction models and assuming the Woodstock Fault (Durá-Gómez and Talwani, 2009a,b) to be the earthquake source. NSHMP = National Seismic Hazard Model Project (Petersen et al., 2014, 2020).

5.7 Forward Predictions of an 1886-Like Rupture

Based on the preceding, which indicated that the intensity and liquefaction data alone cannot well constrain the source of the 1886 event beyond a general region, we forward predict the median PGAs expected in an “1886-like” rupture. As part of this effort, two fault locations and three magnitudes are considered. The purpose of these predictions is to: (i) further illustrate why constraint of the source model is difficult, given data limitations; and (ii) provide predictions for this scenario event using the latest predictive models, which may be useful for regional-scale consequence modelling or science communication. Shown in Figure 17, for example, are predictions considering an $M_w 7.1$ rupture and two strike-slip fault scenarios: (i) fault 1, which is similar to the Woodstock fault; and (ii) fault 2, which is further east, perpendicular to fault 1, and similar to hypothetical faults that were shown to have high likelihoods of producing the MMI and liquefaction evidence (see Figures 9 and 14). Among previously hypothesized sources of the 1886 earthquake, fault 2 is most similar to the Deer Park lineament proposed by Marple and Hurd (2020). Although the predicted PGAs do differ in the nearfield (e.g., within 50 km of the source), the overall expectation at regional scale is obviously similar. Importantly, and as previously discussed, the Bakun et al. (2002) dataset does not contain an abundance of 1886 MMI observations in the vicinity of Charleston, or in the near field more generally. Only 16 observations, for example, are within 100 km of Charleston. As a result, the predicted PGAs, and by corollary MMIs, are relatively similar at most observation sites.

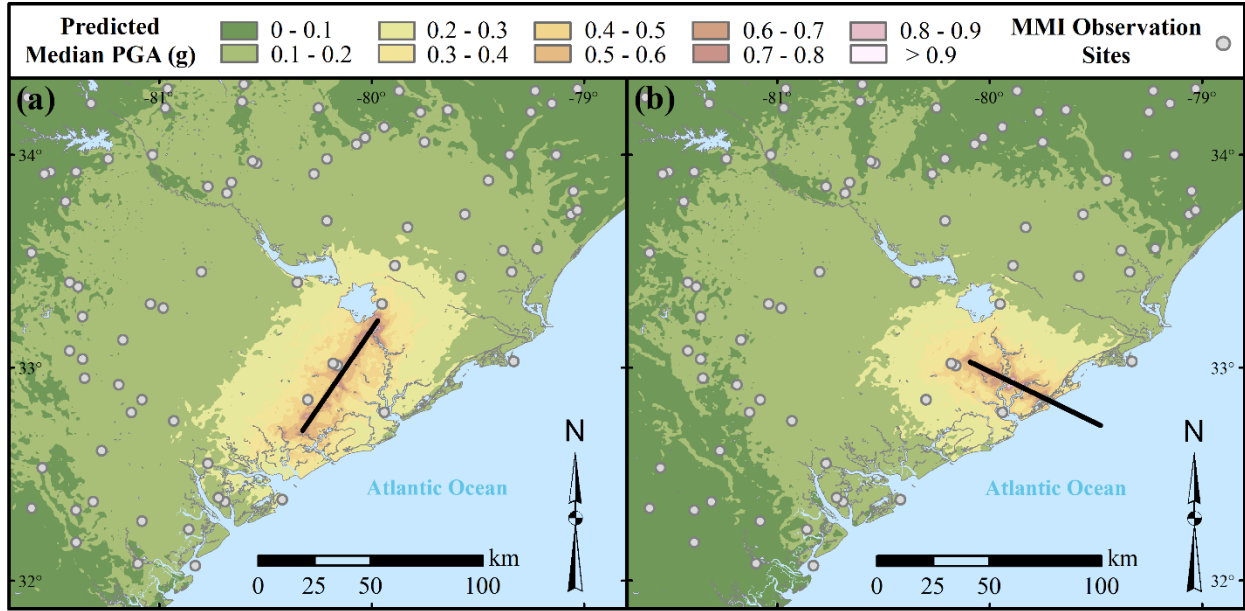


Figure 17. Predictions of median PGA in the Charleston region, as computed using 17 NGA-East GMMs (Goulet et al., 2018) and the Harmon et al. (2019) site-response model, and considering an $M_w 7.1$ rupture on: (a) fault scenario 1; and (b) fault scenario 2, as described in the text.

Plotted in Figure 18, considering these two fault scenarios, are the predicted MMIs at each of the intensity report locations in the Bakun et al. (2002) dataset. For this example, the Atkinson and Kaka (2007) IM-MMI model was adopted. It can be seen that large differences between the predicted MMIs (say, > 0.5 MMI) are rare. In turn, the difficulty of source-model constraint is apparent, given that the two scenarios lead to perceptible differences at relatively few observation sites. While an analogous plot at sites of liquefaction evidence would show larger differences between expected PGAs (given that all such sites are in the near field), the large finite-sample uncertainty of this smaller dataset leads to a similar outcome, with a variety of faults having relatively high likelihoods of producing the evidence (see Figure 14). It follows that additional near-field evidence (whether MMI or liquefaction) could be especially influential to future studies of the 1886 earthquake. Following the same approach, predictions were made for $M_w 6.6$ and $M_w 7.6$ ruptures. These results are shown in the electronic supplement, where each of the forward predictions is also provided as a GIS map package.

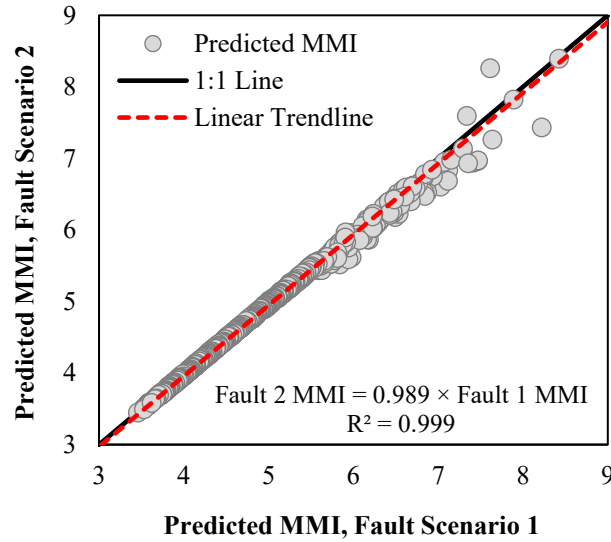


Figure 18. Predictions of MMI using the Atkinson and Kaka (2007) IM-MMI model for fault scenarios 1 and 2 with rupture magnitude $M_w 7.1$. Black line = 1:1 line; red dashed line = linear trendline.

5.8 Limitations and Uncertainties

The findings presented herein are inherently tied to the field evidence currently available and adopted for analysis. Reinterpretation or augmentation of these observations, which we assume to be independent events, would potentially change these findings, as would the adoption of new component models (e.g., to predict ground motions, site response, MMI, liquefaction triggering, or liquefaction manifestation). Undoubtedly, the modeling of these phenomena will continually advance, warranting future analyses of the 1886 Charleston earthquake. ENA ground-motion modeling has advanced, for example, yet GMMs remain especially uncertain and untested at large magnitudes and will continue to evolve. And, as a supplement to empirical GMMs, physics-based ground motion simulations could provide new insights into the 1886 rupture via more explicit modeling of influential site, path, and source effects (e.g., stress drop), as has been shown for other historical earthquakes (e.g., Lozos, 2016). While empirical GMMs are ubiquitous in earthquake science/engineering and implicitly account for many salient effects, a more explicit accounting could help to reduce uncertainty. Moreover, the goal of this study was to assess the degree to which macroseismic evidence can constrain the 1886 source model, rather than to perform a broad investigation of all geophysical and modern seismological evidence, which would fall under the purview of other investigators with different expertise. In addition, it should be noted that many, but not all, sources of uncertainty were accounted for in the analyses. Neglected, for example, were the uncertainties of site characterization (i.e., V_{s30}) and site observations (i.e., MMI and liquefaction responses). The inclusion of these and other uncertainties could potentially broaden the M_w CDFs computed herein. It must similarly be emphasized that a thorough reinterpretation of the more than 1000 original intensity reports, to include the

assignment of site-specific uncertainties, bias corrections, and/or weighting schemes, could potentially change the results we present. And, as previously emphasized, our ensemble M_w CDFs utilize judgement-based weighting schemes. While justifications were provided for these weights, readers might argue for other weights, and thus draw other conclusions from our suites of M_w CDFs. Ultimately, future analyses will confirm or revise the conclusions reached in this study and summarized below.

6. Conclusions

Prior studies of MMI and liquefaction data resulting from the 1886 Charleston, SC, earthquake have several limitations. Namely, these studies tend to: (i) either be deterministic or account for uncertainties in an informal manner (e.g., it is often unclear what published uncertainty bounds represent and which uncertainties are, and are not, included); (ii) assume that the 1886 event was caused by a particular fault (i.e., the Woodstock Fault) without investigating the uncertainty of this assumption or the ability of the field data to constrain source traits beyond magnitude (i.e., fault location, geometry); and (iii) rely on models for predicting various phenomena (e.g., ground motions, site response, liquefaction response, MMI) that have since been superseded or augmented (e.g., by the NGA East project's 17 GMMs). Accordingly, this study presented probabilistic seismic-source inversions of the 1886 earthquake using the latest predictive models and a novel inversion methodology. With this approach, the likelihood of a rupture with some magnitude, location, and geometry to produce a set of field observations is computed. Repeating for enumerable hypothetical sources results in a regional scale constraint of the likely source traits, to the extent that observational data permits. With this approach, magnitude probability distributions conditioned on both an unknown source and on the hypothesized Woodstock Fault (Durá-Gómez and Talwani, 2009a,b) were computed and compared to that used in the U.S. NSHMP (Petersen et al., 2014, 2020). The most salient findings of this study, subject to the limitations and uncertainties summarized in section 5.8, are:

- Neither the location nor orientation of the 1886 fault rupture could be confidently constrained by the macroseismic evidence and models utilized herein, given the large uncertainties inherent to each. Hypothetical faults in a range of locations and with various alignments were deemed to have high relative likelihoods of producing this evidence. Considering both types of evidence and all analyses, faults striking SE and partly offshore were predominantly identified as having the greatest likelihood. Yet these faults ranged in location and other faults, with very different strikes, were also often found to be relatively likely.
- Collectively, the evidence does not provide strong support for the hypothesized Woodstock Fault. One analysis (that of MMI data using the WEA12 IM-MMI model) found a NE-striking “Woodstock like” fault to be the most likely source of the field evidence. Yet most analyses – in so far as supporting the Woodstock Fault – point to the likelihood of a seismic source somewhere north of

Charleston but deem the Woodstock Fault to be relatively unlikely. This is not to say the fault does not exist (geophysical investigations and modern seismological data clearly suggest that many faults exist in the area), but rather, that many aspects of the 1886 source model cannot be well constrained with the available macroseismic evidence and models. This result might change if: (i) more MMI and liquefaction evidence were available – particularly in the near field; (ii) the MMI evidence was reinterpreted to remove or correct outliers, and to assign observation-specific uncertainties; or (iii) if the various required component models were less uncertain.

- In the absence of these developments, certain aspects of the 1886 fault rupture can only be constrained with other seismologic, geologic, and/or coseismic data and interpretation.
- When conditioned on the Woodstock Fault proposed by Durá-Gómez and Talwani (2009a,b), and generally supported by others, our preferred CDF of M_w inverted from MMI data has a median of $M_w 7.10$ and 95% CI of $M_w 7.0$ to $M_w 7.75$. Of all uncertainties considered, the epistemic uncertainty of IM-MMI model selection was larger than any other, since different models may give significantly different MMI predictions for a given IM. In this regard, efforts to better quantify the suitability of IM-MMI models to the study region, and in turn, to refine the weighting scheme used herein, could have a significant influence on our overall conclusions.
- The results from MMI analysis show some site-to-source distance bias, with magnitudes inverted from more distal MMI observations tending to be larger. Possible reasons for this bias were discussed but could be further investigated in the future.
- When conditioned on the Woodstock Fault, our preferred CDF of M_w inverted from liquefaction data has a median of $M_w 7.20$ and 95% CI of $M_w 6.30$ to $M_w 8.10$. The greater M_w uncertainty, relative to that from MMI analysis, is attributable to there being fewer liquefaction study sites, the compilation of which requires both an observation of liquefaction response *and* subsurface geotechnical testing. In addition, the uncertainties of whether and how to correct for soil-aging effects considerably augmented the uncertainty. As such, efforts to quantify the suitability and uncertainties of aging-correction models could have significant influence on our overall conclusions.
- When conditioned on an unknown seismic source, the CDFs of M_w inverted from MMI and liquefaction data did not differ greatly from the CDFs conditioned on the Woodstock Fault. Our interpretation is that while faults with a range of locations and alignments were found similarly likely to produce the field evidence, these faults were inferred to have mostly similar magnitude distributions. Thus, the results of this study pertaining to the magnitude of the 1886 rupture would not necessarily change if the rupture's exact position was known. This should not be interpreted to mean that the uncertainties of source location and geometry are inconsequential to inverse-analyses of macroseismic data. As demonstrated via simulated inversions of modern earthquakes (Rasanen

and Maurer, 2021, 2022), these uncertainties are often considerable. This is especially the case, for example, when the effects of a distant, large M_w rupture cannot be distinguished from the effects of a nearby, small M_w rupture. In such cases, constraint of the source location can dramatically reduce the overall uncertainty of the inverted magnitude.

- Collectively, the results largely support the M_w distribution adopted by the NSHMP, which ranges from $M_w 6.7$ to $M_w 7.5$ with a median of $M_w 7.1$. While analyses indicate that $M_w < 6.7$ ruptures have potential to produce the observed liquefaction response (particularly when the uncertainty of selecting an aging-correction model is considered), the MMI evidence suggests a near-zero likelihood of such magnitudes. Conversely, both types of evidence suggest that $M_w > 7.5$ events have potential to produce the field evidence. While this conclusion hinges on which component models are adopted to predict soil-aging effects and MMI, we fail to find conclusive evidence for outright rejecting some models in favor of others. In the absence of such evidence, the possibility of $M_w > 7.5$ ruptures would merit consideration.
- Ultimately, the flexible inversion methodology employed herein is not specific to ENA, or to certain types of macroseismic evidence, but rather is applicable to any seismic zone and to any co-seismic response for which probabilistic prediction models exist. This methodology allows for uncertainty to be accounted for in a more complete and transparent manner when inverting seismic parameters from macroseismic evidence.

Declaration of competing interests

The authors declare no competing interests.

Acknowledgements

The presented study is based on work supported by the National Science Foundation (NSF) under Grant No. CMMI-1751216 and by the NSF Graduate Research Fellowship Program under Grant No. DGE-1762114. However, any opinions, findings, and conclusions or recommendations expressed in this paper are those of the authors and do not necessarily reflect the views of NSF. We also gratefully acknowledge Silvia Mazzoni of the John Garrick Institute for Risk Sciences at UCLA for developing NGA East ground motion characterization tools based on the results of Goulet et al. (2018), which were utilized in this study.

Appendix A. Supplementary data

All data and models utilized in this study are publicly available, as cited herein. The supplemental material includes 8 additional figures that pertain to the analysis of MMI data using the “epicenter search” and “fault search” methods. The results presented in these figures are summarized and discussed in 5.1-5.2. Also

included are maps (figures and GIS files) of the predicted median PGAs in an “1886-like” event, considering three magnitudes and two fault alignments.

REFERENCES

- Amick, D., G. Maurath, and R. Gelinas (1990). Characteristics of seismically induced liquefaction sites and features located in the vicinity of the 1886 Charleston, South Carolina earthquake, *Seismological Research Letters*, **61**, no. 2, 117-211.
- Andrus R.D., H. Hayati, and N.P. Mohanan (2009). Correcting liquefaction resistance for aged sands using measured to estimated velocity ratio, *J. Geotech. Geoenviron. Eng.*, **135**, no. 6, 735-744, doi: [10.1061/\(ASCE\)GT.1943-5606.0000025](https://doi.org/10.1061/(ASCE)GT.1943-5606.0000025)
- Atkinson G.M., and S.I. Kaka (2007). Relationships between felt intensity and instrumental ground motion in the central United States and California, *Bull. Seismol. Soc. Am.* **97**, no. 2, 497-510, doi: [10.1785/0120060154](https://doi.org/10.1785/0120060154)
- Atkinson, G.M., C.B. Worden, and D.J. Wald (2014). Intensity prediction equations for North America, *Bulletin of the Seismological Society of America*, **104**, no. 6, 3084-3093, doi: [10.1785/0120140178](https://doi.org/10.1785/0120140178)
- Bakun W.H., and M.G. Hopper (2004). Magnitudes and locations of the 1811-1812 New Madrid, Missouri, and the 1886 Charleston, South Carolina, earthquakes, *Bulletin of the Seismological Society of America*, **94**, no. 1, 64-75, doi: [10.1785/0120020122](https://doi.org/10.1785/0120020122).
- Bakun W.H., A.C. Johnston, and M.G. Hopper (2002). Modified Mercalli Intensities (MMI) for large earthquakes near New Madrid, Missouri, in 1811-1812 and near Charleston, South Carolina, in 1886, *U.S. Geol. Surv. Open File Rep.* 02-184.
- Boller, R. (2008). Geotechnical investigations at three sites in the South Carolina coastal plain that did not liquefy during the 1886 Charleston earthquake (*Master's thesis*). Available from https://tigerprints.clemson.edu/all_theses/301/
- Bollinger, G.A. (1977). Reinterpretation of the intensity data for the 1886 Charleston, South Carolina, earthquake, *U.S. Geol. Surv. Profess. Pap.* 1028, 17-32.
- Bollinger, G.A. and C.W. Stover (1976). List of intensities for the 1886 Charleston, South Carolina earthquake, *U.S. Geol. Surv. Open-File Rept.* 76-66, 31pp.
- Bommer, J.J., B. Dost, B. Edwards, P.J. Stafford, J. van Elk, D. Doornhof, and M. Ntinalexis (2016). Developing an application-specific ground motion model for induced seismicity, *Bull. Seismol. Soc. Am.* **106**, 158–173, doi: [10.1785/0120150184](https://doi.org/10.1785/0120150184)
- Boulanger R.W., and I.M. Idriss (2014). CPT and SPT based liquefaction triggering procedures. Report no. UCD/CGM-14/01. Davis, CA: Center for Geotechnical Modeling, University of California, Davis.
- Bwambale, B., Andrus, R. D., Heidari, T., Gathro, J., & Cramer, C. H. (2022). Influence of source-to-site distance and diagenesis on liquefaction triggering of 200,000-year-old beach sand. *Engineering Geology*, 298, 106557, [10.1016/j.enggeo.2022.106557](https://doi.org/10.1016/j.enggeo.2022.106557).
- Caprio M., B. Tarigan, C.B. Worden, S. Wiemer, and D.J. Wald (2015). Ground motion to intensity conversion equations (GMICEs): A global relationship and evaluation of regional dependency, *Bull. Seismol. Soc. Am.* **105**, no. 3, 1476-1490, doi: [10.1785/0120140286](https://doi.org/10.1785/0120140286)
- Chapman, M.C., M.S. Sibol, and G. A. Bollinger (1989). Investigation of anomalous earthquake intensity levels along the coastal-plain-Piedmont boundary in South Carolina and Georgia, *Virginia Tech Seismological Observatory Report* 1360.
- Chapman, M.C., J.N. Beale, A.C. Hardy, and Q. Wu (2016). Modern seismicity and the fault responsible for the 1886 Charleston, South Carolina, earthquake, *Bulletin of the Seismological Society of America*, **106**, no. 2, 364-372, doi: [10.1785/0120150221](https://doi.org/10.1785/0120150221).
- Chung, J., Okok, A., and Rogers, J. D. (2021). Geologic impacts and calculated magnitudes of historic earthquakes in the central United States. *Engineering Geology*, 280, 105923, doi: [10.1016/j.enggeo.2020.105923](https://doi.org/10.1016/j.enggeo.2020.105923).

- Coppersmith, K. J., Salomone, L. A., Fuller, C. W., Glaser, L. L., Hanson, K. L., Hartleb, R. D., ... & Tuttle, M. P. (2012). Central and eastern United States (CEUS) seismic source characterization (SSC) for nuclear facilities project (No. DOE/NE-0140). Electric Power Research Institute (EPRI).
- Cramer, C.H. (2020). Updated GMICE for central and eastern North America extending to higher intensities, *Seimol. Res. Lett.* **91**, no. 6, 3518-3527, doi: [10.1785/0220200061](https://doi.org/10.1785/0220200061)
- Cramer, C.H., and O.S. Boyd (2014). Why the New Madrid earthquakes are M 7-8 and the Charleston earthquake is $\sim M$ 7, *Bulletin of the Seismological Society of America*, **104**, no. 6, 2884-2903, doi: [10.1785/0120120257](https://doi.org/10.1785/0120120257)
- de Magistris, F.S., G. Lanzano, G. Forte, and G. Fabbrocino (2013). A database for PGA threshold in liquefaction occurrence, *Soil Dynamics and Earthquake Engineering*, **54**, 17-19, doi: [10.1016/j.soildyn.2013.07.011](https://doi.org/10.1016/j.soildyn.2013.07.011)
- Durá-Gómez, I., and P. Talwani (2009a). Finding faults in the Charleston area, South Carolina: 1. seismological data. *Seismological Research Letters* **80**, no. 5, 883-900, doi: [10.1785/gssrl.80.5.883](https://doi.org/10.1785/gssrl.80.5.883)
- Durá-Gómez, I., and P. Talwani (2009b). Finding faults in the Charleston area, South Carolina: 2. complementary data. *Seismological Research Letters* **80**, no. 5, 901-919, doi: [10.1785/gssrl.80.5.901](https://doi.org/10.1785/gssrl.80.5.901)
- Dutton, C.E. (1889). The Charleston earthquake of August 31, 1886: *U.S. Geological Survey*, Ninth Annual Report 1887-88, 203-528.
- Gheibi, E., & Gassman, S. L. (2016). Application of GMPEs to estimate the minimum magnitude and peak ground acceleration of prehistoric earthquakes at Hollywood, SC. *Engineering Geology*, **214**, 60-66, doi: [10.1016/j.enggeo.2016.09.016](https://doi.org/10.1016/j.enggeo.2016.09.016).
- Geiger, A. (2010). Liquefaction analysis of three Pleistocene sand deposits that did not liquefy during the 1886 Charleston, South Carolina earthquake based on shear wave velocity and penetration resistance (*Master's thesis*). Available from https://tigerprints.clemson.edu/all_theses/815/
- Geyin M. and B.W. Maurer (2020). Fragility functions for liquefaction-induced ground failure, *Journal of Geotechnical and Geoenvironmental Engineering* **146**, no. 12, doi: [10.1061/\(ASCE\)GT.1943-5606.0002416](https://doi.org/10.1061/(ASCE)GT.1943-5606.0002416)
- Gheibi, E., S. Gassman, and P. Talwani (2020). Regional assessment of prehistoric earthquake magnitudes in the South Carolina Coastal Plain, *Bulletin of Engineering Geology and the Environment*, **79**, no. 3, 1413-1427, doi: [10.1007/s10064-019-01627-7](https://doi.org/10.1007/s10064-019-01627-7)
- Gohn, G.S., R.E. Weems, S.F. Obermeier, and R.L. Gelinas (1984). Field studies of earthquake-induced liquefaction-flowage features in the Charleston, South Carolina area: preliminary report: *U.S. Geological Survey Open-File Report* 84-670, 26 p.
- Goulet, C., Y. Bozorgnia, N. Abrahamson, N. Kuehn, L. Al Atik, R. Youngs, R.W. Graves, G.M. Atkinson (2018). Central and eastern North America ground-motion characterization (NGA-East Final Report, PEER Report Number 2018/08). Berkeley, CA: Pacific Earthquake Engineering Research Center, University of California.
- Green, R.A., J.J. Bommer, A. Rodriguez-Marek, B.W. Maurer, P.J. Stafford, B. Edwards, ... J., Van Elk (2019). Addressing limitations in existing 'simplified' liquefaction triggering evaluation procedures: application to induced seismicity in the Groningen gas field. *Bulletin of Earthquake Engineering*, **17**, no. 8, 4539-4557. doi: [10.1007/s10518-018-0489-3](https://doi.org/10.1007/s10518-018-0489-3)
- Harmon, J., Y.M.A., Hashash, J.P. Stewart, E.M. Rathje, K.W. Campbell, W.J. Silva, and O. Ilhan (2019). Site Amplification Functions for Central and Eastern North America – Part II: Modular Simulation-Based Models, *Earthquake Spectra*, **35**, no. 2, 815-847, doi: [10.1193/091117EQS179M](https://doi.org/10.1193/091117EQS179M)
- Hasek, M.J. (2016). Age-related liquefaction resistance of Pleistocene coastal plain sands in South Carolina (*Doctoral dissertation*). Retrieved from <https://scholarcommons.sc.edu/etd/3600>.
- Hayati, H. and R.D. Andrus (2008). Liquefaction potential map of Charleston, South Carolina based on the 1886 earthquake, *Journal of Geotechnical and Geoenvironmental Engineering*, **134**, no. 6, 815-828, doi: [10.1061/\(ASCE\)1090-0241\(2008\)134:6\(815\)](https://doi.org/10.1061/(ASCE)1090-0241(2008)134:6(815))

- Hayati, H., and R.D. Andrus (2009). Updated liquefaction resistance correction factors for aged soils, *Journal of Geotechnical and Geoenvironmental Engineering*, **135**, no. 11, 1683–1692, doi: [10.1061/\(ASCE\)GT.1943-5606.0000118](https://doi.org/10.1061/(ASCE)GT.1943-5606.0000118)
- Heidari, T., and R.D. Andrus (2010). Mapping liquefaction potential of aged soil deposits in Mount Pleasant, South Carolina, *Eng. Geol.* **112**, 1–12, doi: [10.1016/j.enggeo.2010.02.001](https://doi.org/10.1016/j.enggeo.2010.02.001)
- Heidari, T., and R.D. Andrus (2012). Liquefaction potential assessment of Pleistocene beach sands near Charleston, South Carolina, *J. Geotech. Geoenviron. Eng.* **138**, no. 10, 1196–1208, doi: [10.1061/\(ASCE\)GT.1943-5606.0000686](https://doi.org/10.1061/(ASCE)GT.1943-5606.0000686)
- Heath, D.C., D.J. Wald, C.B. Worden, E.M. Thompson and G.M. Smoczyk (2020) A global hybrid Vs30 map with a topographic slope-based default and regional map insets. *Earthquake Spectra* **36**, 1570–1584, doi: [10.1177/8755293020911137](https://doi.org/10.1177/8755293020911137)
- Hough, S. E., Armbruster, J. G., Seeber, L., and Hough, J. F. (2000). On the modified Mercalli intensities and magnitudes of the 1811–1812 New Madrid earthquakes. *Journal of Geophysical Research: Solid Earth*, **105**(B10), 23839–23864.
- Hu, K., S.L. Gassman, and P. Talwani (2002). Magnitudes of prehistoric earthquakes in the South Carolina coastal plain from geotechnical data, *Seismological Research Letters*, **73**, no. 6, 979–991, doi: [10.1061/9780784479087.112](https://doi.org/10.1061/9780784479087.112)
- Ishihara, K. (1985). Stability of natural soil deposits during earthquakes, *Proc. 11th Conf. on Soil Mech. and Found. Engrg.*, International Society of Soil Mechanics and Foundation Engineers, San Francisco, Calif., 321–376.
- Iwasaki T., F. Tatsuoka, K. Tokida and S. Yasud (1978) A practical method for assessing soil liquefaction potential based on case studies at various sites in Japan. In: Proceedings of the 2nd international conference on microzonation for safer construction research and application, (2): 885–896, 30 Oct– 3 Nov, Seattle, Washington.
- Johnston, A.C. (1996). Seismic moment assessment of stable continental earthquakes - III. New Madrid 1811–1812, Charleston 1886 and Lisbon 1755, *Geophys. J. Int.*, **126**, no. 2, 314–344, doi: [10.1111/j.1365-246X.1996.tb05294.x](https://doi.org/10.1111/j.1365-246X.1996.tb05294.x)
- Kaklamanos J., L.G. Baise and D.M. Boore (2011). Estimating unknown input parameters when implementing the NGA ground motion prediction equations in engineering practice, *Earthquake Spectra* **27**, no. 4, 1219–1235, doi: [10.1193/1.3650372](https://doi.org/10.1193/1.3650372)
- Kuhn, G. G. (2005). Paleoseismic features as indicators of earthquake hazards in North Coastal, San Diego County, California, USA. *Engineering geology*, **80**(1-2), 115–150, doi: [10.1016/j.enggeo.2005.04.006](https://doi.org/10.1016/j.enggeo.2005.04.006).
- Lozos, J.C. (2016). A case for historic joint rupture of the San Andreas and San Jacinto faults. *Science advances*, **2**(3), e1500621.
- Marple, R. T., & Hurd, J. D. (2020). Interpretation of lineaments and faults near Summerville, South Carolina, USA, using LiDAR data: Implications for the cause of the 1886 Charleston, South Carolina, earthquake. *Atlantic Geology: Journal of the Atlantic Geoscience Society/Atlantic Geology: revue de la Société Géoscientifique de l'Atlantique*, **56**, 73–95, doi: [10.4138/atlgol.2020.003](https://doi.org/10.4138/atlgol.2020.003).
- Martin, J.R., II, and G.W. Clough (1994). Seismic parameters from liquefaction evidence, *J. Geotech. Engrg.*, **120**, no. 8, 1345–1361, doi: [10.1061/\(ASCE\)0733-9410\(1994\)120:8\(1345\)](https://doi.org/10.1061/(ASCE)0733-9410(1994)120:8(1345))
- Maurer, B.W., R.A. Green, M. Cubrinovski, and B.A. Bradley (2014). Assessment of aging correction factors for liquefaction resistance at sites of recurrent liquefaction. In *Proceedings of the 10th US National Conference on Earthquake Engineering*.
- Maurer, B. W., Green, R. A., Quigley, M. C., & Bastin, S. (2015a). Development of magnitude-bound relations for paleoliquefaction analyses: New Zealand case study. *Engineering Geology*, **197**, 253–266, doi: [10.1016/j.enggeo.2015.08.023](https://doi.org/10.1016/j.enggeo.2015.08.023).
- Maurer, B.W., R.A. Green, and O.D.S Taylor (2015b). Moving towards an improved index for assessing liquefaction hazard: lessons from historical data. *Soils and Foundations*, **55**, no. 4, 778–787. doi: [10.1016/j.sandf.2015.06.010](https://doi.org/10.1016/j.sandf.2015.06.010)

- Nuttl, O.W., G.A. Bollinger, and R.B. Herrmann (1986). The 1886 Charleston, South Carolina, earthquake: A 1986 perspective, *U.S. Geological Survey*, **985**, doi: [10.3133/cir985](https://doi.org/10.3133/cir985)
- Obermeier, S. F. (1998). Liquefaction evidence for strong earthquakes of Holocene and latest Pleistocene ages in the states of Indiana and Illinois, USA. *Engineering Geology*, *50*(3-4), 227-254, doi: [10.1016/S0013-7952\(98\)00032-5](https://doi.org/10.1016/S0013-7952(98)00032-5).
- Obermeier, S.F., G.S. Gohn, R.S. Weems, R.L. Gelinas, and M. Rubin (1985). Geologic Evidence for Recurrent Moderate to Large Earthquakes Near Charleston, South Carolina, *Science*, **277**, no. 4685, 408-411.
- Obermeier, S. F., Olson, S. M., & Green, R. A. (2005). Field occurrences of liquefaction-induced features: a primer for engineering geologic analysis of paleoseismic shaking. *Engineering Geology*, *76*(3-4), 209-234, doi: [10.1016/j.enggeo.2004.07.009](https://doi.org/10.1016/j.enggeo.2004.07.009).
- Obermeier, S. F., R.E. Weems, and R.B. Jacobson, (1987). Earthquake induced liquefaction features in the coastal South Carolina region, *U.S. Geol. Surv. Open File Report* 87-504.
- Olson, S. M., Green, R. A., & Obermeier, S. F. (2005). Geotechnical analysis of paleoseismic shaking using liquefaction features: a major updating. *Engineering Geology*, *76*(3-4), 235-261, doi: [10.1016/j.enggeo.2004.07.008](https://doi.org/10.1016/j.enggeo.2004.07.008).
- Petersen, M.D., M.P. Moschetti, P.M. Powers, C.S. Mueller, K.M. Haller, A.D. Frankel, ... A.H. Olsen (2014). Documentation for the 2014 update of the United States national seismic hazard maps. *U.S. Geol. Surv. Open-File Report* 2014-1091.
- Petersen, M.D., A.M. Shumway, P.M. Powers, C.S. Mueller, M.P. Moschetti, A.D. Frankel, ... Y. Zeng (2020). The 2018 update of the US National Seismic Hazard Model: Overview of model and implications, *Earthquake Spectra*, **36**, no. 1, 5-41, doi: [10.1177/8755293019878199](https://doi.org/10.1177/8755293019878199)
- Pratt, T. L., Shah, A. K., Counts, R. C., Horton, J. W., & Chapman, M. C. (2022). Shallow Faulting and Folding in the Epicentral Area of the 1886 Charleston, South Carolina, Earthquake. *Bulletin of the Seismological Society of America*, doi: [10.1785/0120210329](https://doi.org/10.1785/0120210329).
- Rasanen, R.A., and B.W. Maurer (2021). Probabilistic seismic source inversion from regional landslide evidence. *Landslides*, doi: [10.1007/s10346-021-01780-9](https://doi.org/10.1007/s10346-021-01780-9)
- Rasanen, R.A., and B.W. Maurer (2022). Probabilistic seismic source location and magnitude via inverse analysis of paleoliquefaction evidence. *Earthquake Spectra*, *In Press*.
- Rasanen, R. A., Marafi, N. A., & Maurer, B. W. (2021). Compilation and forecasting of paleoliquefaction evidence for the strength of ground motions in the US Pacific Northwest. *Engineering Geology*, *292*, 106253, doi: [10.1016/j.enggeo.2021.106253](https://doi.org/10.1016/j.enggeo.2021.106253).
- Robertson, P.K., and C.E. Wride (1998). Evaluating cyclic liquefaction potential using the cone penetration test. *Canadian Geotechnical Journal*, **35**, no. 3, 442-459. doi: [10.1139/t98-017](https://doi.org/10.1139/t98-017)
- Rodriguez-Marek, A., & Ciani, D. (2008). Probabilistic methodology for the analysis of paleoliquefaction features. *Engineering geology*, *96*(3-4), 159-172, [10.1016/j.enggeo.2007.10.007](https://doi.org/10.1016/j.enggeo.2007.10.007).
- Scherbaum F., J. Schmedes and F. Cotton (2004). On the conversion of source-to-site distance measures for extended earthquake source models. *Bulletin of the Seismological Society of America* **94**, no. 3, 1053-1069, doi: [10.1785/0120030055](https://doi.org/10.1785/0120030055)
- Schneider, J. A., Mayne, P. W., & Rix, G. J. (2001). Geotechnical site characterization in the greater Memphis area using cone penetration tests. *Engineering Geology*, *62*(1-3), 169-184, doi: [10.1016/S0013-7952\(01\)00060-6](https://doi.org/10.1016/S0013-7952(01)00060-6).
- Seed, H.B., K. Tokimatsu, L.F. Harder, and R.M. Chung (1984). The influence of SPT procedures in soil liquefaction resistance evaluations, *Report No. UBC/EERC-84/15*, Earthquake Engineering Research Center, University of California, Berkeley, Calif.
- Silva, W., I. Wong, T. Siegel, N. Gregor, R. Darragh, and R. Lee (2003). Ground motion and liquefaction simulation of the 1886 Charleston, South Carolina, earthquake, *Bulletin of the Seismological Society of America*, **93**, no. 6, 2717-2736, doi: [10.1785/0120030029](https://doi.org/10.1785/0120030029)

- Stover, C.W. and J.L. Coffman (1993). Seismicity of the United States, 1568-1989 (Revised), *U.S. Geological Survey Prof. Pap.* 1527, 418pp.
- Talwani, P., and J. Cox (1985). Paleoseismic evidence for recurrence of earthquakes near Charleston, South Carolina, *Science*, **228**, no. 4711, 379-381, doi: [10.1126/science.229.4711.379](https://doi.org/10.1126/science.229.4711.379)
- Talwani, P., M. Hasek, S. Gassman, W.R. Doar III, and A. Chapman (2011). Discovery of a sand blow and associated fault in the epicentral area of the 1886 Charleston earthquake, *Seismological Research Letters*, **82**, no. 4, 589-598, doi: [10.1785/gssrl.82.4.589](https://doi.org/10.1785/gssrl.82.4.589)
- Talwani, P., and W.T. Schaeffer (2001). Recurrence rates of large earthquakes in the South Carolina coastal plain based on paleoliquefaction data, *Journal of Geophysical Research*, **106**, no. B4, 6621-6642, doi: [10.1029/2000JB900398](https://doi.org/10.1029/2000JB900398)
- Thompson, E. M., and C.B. Worden (2018). Estimating rupture distances without a rupture. *Bulletin of the Seismological Society of America*, **108**, no. 1, 371-379, doi: [10.1785/0120170174](https://doi.org/10.1785/0120170174)
- USGS (2022). Advanced National Seismic System (ANSS) Comprehensive Catalog of Earthquake Events and Products: Various. U.S. Geological Survey, Earthquake Hazards Program. doi: [10.5066/F7MS3QZH](https://doi.org/10.5066/F7MS3QZH)
- Weems, R.E., W.C. Lewis, and E.M. Lemon, Jr. (2014). Surficial geologic map of the Charleston region, Berkeley, Charleston, Colleton, Dorchester, and Georgetown Counties, South Carolina, *U.S. Geological Survey Open-File Report* 2013–1030, 1 sheet, scale 1:100,000, doi: [10.3133/ofr20131030](https://doi.org/10.3133/ofr20131030)
- Wells D.L., and K.J. Coppersmith (1994). New empirical relationships among magnitude, rupture length, rupture width, rupture area, and surface displacement. *Bull. Seismol. Soc. Am.* **84**, no. 4, 974–1002, doi: [10.1785/BSSA0840040974](https://doi.org/10.1785/BSSA0840040974)
- Werner, M. J., and D. Sornette (2008). Magnitude uncertainties impact seismic rate estimates, forecasts, and predictability experiments, *J. Geophys. Res.*, **113**, no. B8, doi: [10.1029/2007JB005427](https://doi.org/10.1029/2007JB005427)
- Williamson, J.R., and S.L. Gassman (2014). Identification of liquefiable coastal plain soils using DMT, SPT, and CPT profiles, *Geo-Congress 2014*, February 23-26, Atlanta, Georgia, doi: [10.1061/9780784413272.206](https://doi.org/10.1061/9780784413272.206)
- Wong, I., J. Bouabid, W. Graf, C. Huyck, A. Porush, W. Silva, T. Siegel, G. Bureau, R. Eguchi, and J. Knight (2005). Potential losses in a repeat of the 1886 Charleston, South Carolina, earthquake, *Earthquake Spectra*, **21**, no. 4, 1157-1184, doi: [10.1193/1.2083907](https://doi.org/10.1193/1.2083907).
- Wood, H.O., and F. Neumann (1931). Modified Mercalli Intensity scale of 1931, *Bull. Seismol. Soc. Am.* **21**, 277-283.
- Worden, C.B., M.C. Gerstenberger, D.A. Rhoades, and D.J. Wald (2012). Probabilistic relationships between ground-motion parameters and Modified Mercalli Intensity in California, *Bull. Seismol. Soc. Am.* **102**, no. 1, 204-221, doi: [10.1785/0120110156](https://doi.org/10.1785/0120110156).
- Yousuf, M., Bukhari, S. K., & Bhat, G. R. (2021). Using paleo-liquefaction features to determine the likely source, magnitude and ground accelerations of pre-historic earthquakes in the Kashmir Basin (Northwestern Himalaya), India. *Engineering Geology*, 293, 106302, [10.1016/j.enggeo.2021.106302](https://doi.org/10.1016/j.enggeo.2021.106302).